

CRANFIELD UNIVERSITY

JONATHON PARKINS

**HEAT TRANSFER PROPERTIES OF LASER ASSISTED  
PLASMA PROCESSING**

SCHOOL OF APPLIED SCIENCES

Precision Engineering

MSc THESIS

Academic Year: 2011 – 2012

Supervisors: Dr Renaud Jourdain, Professor Paul Shore

August 2012



CRANFIELD UNIVERSITY

SCHOOL OF APPLIED SCIENCES

Precision Engineering

MSc THESIS

Academic Year: 2011 – 2012

JONATHON PARKINS

HEAT TRANSFER PROPERTIES OF LASER ASSISTED PLASMA PROCESSING

Supervisors: Dr Renaud Jourdain, Professor Paul Shore

August 2012

© Cranfield University 2011. All rights reserved. No part of this publication may be reproduced without the written permission of the copyright owner.



## ABSTRACT

Laser assisted plasma processing (LAPP) is a novel extension to already established Reactive Atom Plasma (RAP) processing for atmospheric pressure dry chemical etching of silicon based materials; this is mainly applied for optical uses. The development of the new technology involves the implementation of an additional laser energy beam to tune the thermal footprint of the hybrid tool. This will influence the temperature-dependent etching reaction.

The aim of the project was to develop a model to predict the temperature footprint of components of the LAPP tool and assess the suitability of this model in simulating the thermal effects during an actual process. This was undertaken via two routes: model development and experimental temperature investigation. The two materials investigated were Corning Ultra Low Expansion glass (ULE) and also Silicon Carbide (SiC).

The model was developed using Matlab from an established analytical method and evolved for LAPP use. An analytical method based on a Green's function solution to the heat equation for a moving Gaussian heat source on a surface was chosen as it would be an adaptable and rapid alternative to costly experimental measurements for LAPP.

Experimental temperature measurements were investigated using pyrometers, resistance temperature detectors and thermocouples. Typical LAPP process parameters were investigated for both a laser source and a RAP torch, and the temperature was measured. Additionally, surface reflectivity was measured for appropriate wavelengths for LAPP applications using a Fourier transform infrared spectrometer to determine the absorbed portion of laser energy.

The experimental work conducted using RTDs found strong correlation with the modelling, with 63% of results matching within experimental error. The pyrometer measurements were less successfully replicated, the reason for which is expected to be the cooling of the substrate from its upper surface not being accounted for in the model. Overall trends of temperature rise decreasing with increasing feed speed or decreasing power were observed. Thermocouple characterisation of the RAP torch was approximated using the radiative model.



## ACKNOWLEDGEMENTS

I would like to thank, first and foremost, my supervisors Professor Paul Shore and Dr Renaud Jourdain. Their excellent guidance and experienced input has been an integral part of the project and I owe much of what I have achieved to those two men.

My thanks go to Professor Bill O'Neill and Dr Martin Sparkes at the Institute for Manufacturing, University of Cambridge. The expertise and help with implementation of laser sources they provided were a key part of both laser assisted plasma processing as a concept and also this project.

Dr Silvia Marson and Mr Marco Castelli also have my thanks for their contributions to reactive atom plasma knowledge and nous in operation of the machines. Their involvement of the knowledge and development of this technology were essential in the progress of laser assisted plasma processing.

I would like to thank Dr Debabrata Bhattacharyya for allowing access to equipment and providing support for my spectrometric investigations.

The technicians within Cranfield University Precision Engineering Institute are the people who keep everything running within the department. Thanks to Andrew Eve, Alan Heaume, John Hedge, Kevin Howard and in particular Adam Kerr, without whom the construction of the LAPP machine would not have progressed.

Dr Xavier Tonnellier deserves thanks for the patient advice he supplied along with the lending of expensive silicon carbide substrates for experimental investigation of laser heat transfer.

A brief mention to other staff members who have passed on sage advice or technical expertise through my time at Cranfield: Mr Paul Morantz, Dr Ian Walton, Dr Paul Comley, Dr Chris Sansom, Dr Heather Almond, Mr Keith Carlisle, Mr Andrew Dyer, Dr Paul Colegrove.

Thanks to Anne Fiorucci and Marlene Devonshire for helping out with the administrative aspects and purchase orders that had to be processed for the project to succeed.

Thank you to my parents, Jan and Mike Parkins for supporting me, always being there when the going gets tough.

And finally, a thank you must go to Cranfield University Precision Engineering Institute for the chance to study and further my academic career and to the Integrated Knowledge Centre for supporting the project. This is not taken lightly and I will be always grateful for this opportunity.





## CONTENTS

<b>COVER.....</b>	<b>i</b>
<b>TITLE.....</b>	<b>iii</b>
<b>ABSTRACT .....</b>	<b>v</b>
<b>ACKNOWLEDGEMENTS .....</b>	<b>vii</b>
<b>CONTENTS .....</b>	<b>ix</b>
<b>GLOSSARY .....</b>	<b>1</b>
<b>LIST OF FIGURES.....</b>	<b>2</b>
<b>LIST OF TABLES.....</b>	<b>4</b>
<b>1. INTRODUCTION.....</b>	<b>5</b>
<b>1.1 Context.....</b>	<b>5</b>
<b>1.2 Key objectives and reasoning.....</b>	<b>6</b>
<b>1.3 Thesis structure.....</b>	<b>6</b>
<b>2. LITERATURE REVIEW.....</b>	<b>7</b>
<b>2.1 Plasma principles .....</b>	<b>7</b>
<b>2.2 Surface processing .....</b>	<b>8</b>
<i>2.2.1 Atmospheric plasma .....</i>	<i>8</i>
<i>2.2.2 Other surface processing methods .....</i>	<i>12</i>
<b>2.3 Lasers .....</b>	<b>14</b>
<i>2.3.1 Laser-plasma interactions.....</i>	<i>15</i>
<i>2.3.2 Light-solid matter interactions.....</i>	<i>17</i>
<i>2.3.3 Mathematical Modelling .....</i>	<i>19</i>
<b>2.4 Temperature measurement.....</b>	<b>21</b>
<b>3. MODELLING.....</b>	<b>23</b>
<b>3.1 Analytical model .....</b>	<b>24</b>
<i>3.1.1 Programming detail.....</i>	<i>24</i>
<i>3.1.2 Starting assumptions .....</i>	<i>25</i>
<i>3.1.3 Transformation.....</i>	<i>26</i>
<i>3.1.4 Preliminary assessment.....</i>	<i>27</i>
<b>4. MATERIALS AND METHODS .....</b>	<b>31</b>
<b>4.1 Materials .....</b>	<b>31</b>
<i>4.1.1 Substrates .....</i>	<i>31</i>

4.1.2	<i>Sample preparation</i> .....	31
<b>4.2</b>	<b>Methods</b> .....	<b>32</b>
4.2.1	<i>Spectrometry</i> .....	32
4.2.2	<i>Surface temperature measurement</i> .....	34
4.2.2.1	Resistance temperature detectors .....	34
4.2.2.2	Pyrometers .....	37
4.2.2.3	Thermocouples.....	41
<b>5.</b>	<b>RESULTS AND DISCUSSION</b> .....	<b>44</b>
<b>5.1</b>	<b>Spectrometry</b> .....	<b>44</b>
<b>5.2</b>	<b>RTD results</b> .....	<b>48</b>
<b>5.3</b>	<b>Pyrometer results</b> .....	<b>54</b>
5.3.1	<i>ULE</i> .....	54
5.3.2	<i>SiC</i> .....	57
5.3.3	<i>Errors</i> .....	59
<b>5.4</b>	<b>Thermocouples</b> .....	<b>59</b>
5.4.1	<i>Errors</i> .....	67
<b>6.</b>	<b>CONCLUSIONS AND FUTURE WORK</b> .....	<b>68</b>
<b>6.1</b>	<b>Spectrometry</b> .....	<b>68</b>
<b>6.2</b>	<b>Model development</b> .....	<b>68</b>
<b>6.3</b>	<b>Laser source investigation</b> .....	<b>68</b>
6.3.1	<i>RTDs</i> .....	69
6.3.2	<i>Pyrometers</i> .....	70
<b>6.4</b>	<b>RAP source investigation</b> .....	<b>72</b>
<b>6.5</b>	<b>Additional further work</b> .....	<b>73</b>
<b>7.</b>	<b>REFERENCES</b> .....	<b>75</b>

## GLOSSARY

CO <sub>2</sub>	Carbon Dioxide
CW	Continuous Wave (in reference to laser operation)
E-ELT	European Extremely Large Telescope
EM	Electromagnetic
FEA	Finite Element Analysis
FIB	Focussed Ion Beam
FWHM	Full width at half maximum
ICP	Inductively couple plasma
LAPP	Laser Assisted Plasma Processing
m/min	Metres per minute, unit of feed speed
MR	Magnetorheological
Pt100	100Ω resistance platinum
RAP	Reactive Atom Plasma
RF	Radio frequency
RMS	Root mean square
RTD	Resistance temperature detector
Si	Silicon
SiC	Silicon Carbide
Trex	Brand of silicon carbide
ULE	Corning Ultra-Low Expansion glass
W	Watts, unit of power
ZnSe	Zinc Selenide
1/e <sup>2</sup>	~86% enclosed
σ	Standard deviation
∅	Diameter
μm	Micrometre (10 <sup>-6</sup> m)

## LIST OF FIGURES

Figure 2.1 – Schematic of Inductively Coupled Plasma torch used for Reactive Atom Plasma processing .....	<b>Page 9</b>
Figure 2.2 – Example of a doughnut laser intensity profile .....	<b>Page 15</b>
Figure 2.3 – Plot of critical electron density with wavelength.....	<b>Page 16</b>
Figure 3.1 – Experimental setup for the preliminary results .....	<b>Page 28</b>
Figure 3.2 – Example temperature map on a substrate surface demonstrating pyrometer field of view prediction and ‘Not a Number’ masking.....	<b>Page 29</b>
Figure 4.1 – Images of ULE and SiC substrates instrumented with RTDs .....	<b>Page 32</b>
Figure 4.2 – Optical configuration used for inducing temperature rise on ULE and SiC substrates using focussing optics .....	<b>Page 34</b>
Figure 4.3 – Image of experimental configuration for inducing temperature rise on ULE and SiC substrates including optics, stage set up and sensors.....	<b>Page 35</b>
Figure 4.4 – Diagram of laser paths relative to the ULE and SiC substrate and the corresponding sensors .....	<b>Page 36</b>
Figure 4.5 – Image of experimental setup, focussing on laser incidence on substrate, demonstrating sensors .....	<b>Page 36</b>
Figure 4.6 – Schematic of perpendicular pyrometer configuration presenting field of view and stand-off distance .....	<b>Page 38</b>
Figure 4.7 – Schematic of 45° angled pyrometer configuration demonstrating field of view and physical positioning .....	<b>Page 38</b>
Figure 4.8 – Computer generated diagram of 45° pyrometer configuration positioned over laser incidence zone.....	<b>Page 39</b>
Figure 4.9 – Computer generated diagram of 45° pyrometer configuration positioned 50.4mm displaced from the laser incidence zone.....	<b>Page 39</b>
Figure 4.10 – Image of a sample pyrometer configuration involving 45° pyrometer at 50.4mm displacement and 10mm stand-off perpendicular pyrometer .....	<b>Page 40</b>
Figure 4.11 – Image of a sample pyrometer configuration involving 45° pyrometer over laser incidence zone and 15mm stand-off perpendicular pyrometer .....	<b>Page 40</b>
Figure 4.12 – Image of Si wafer instrumented with thermocouples .....	<b>Page 42</b>

Figure 4.13 – Diagram of thermocouple geometries relative to the plasma torch travel path across the substrate .....	<b>Page 42</b>
Figure 5.1 – Plot of reflectivity with wavelength at 65° incidence angle and spherical diffuse reflection for ULE substrate .....	<b>Page 45</b>
Figure 5.2 – Plot of reflectivity with wavelength at 65° incidence angle and spherical diffuse reflection for Trex SiC substrate .....	<b>Page 46</b>
Figure 5.3 – Plot of reflectivity with wavelength at 65° incidence angle for Trex SiC and also porous SiC substrates .....	<b>Page 47</b>
Figure 5.4 – Plot of temperature with time as measured by RTDs on a ULE substrate, processed at 5m/min, 10W laser power, 2mm spot diameter.....	<b>Page 48</b>
Figure 5.5 – Plot of temperature with time as measured by RTDs on a ULE substrate, processed at 4m/min, 10W laser power, 2mm spot diameter.....	<b>Page 49</b>
Figure 5.6 – Plot of temperature with time as measured by RTDs on a SiC substrate, processed at 0.5m/min, 47.5W laser power, 400µm spot diameter.....	<b>Page 50</b>
Figure 5.7 – Plot of initial raised temperature as measured by pyrometers under various process conditions on a ULE substrate.....	<b>Page 54</b>
Figure 5.8 – Plot of final raised temperature as measured by pyrometers under various process conditions on a ULE substrate.....	<b>Page 55</b>
Figure 5.9 – Comparison of temperature induced on SiC square substrate by 35W and 47.5W laser power with time.....	<b>Page 57</b>
Figure 5.10 – Plot of temperature induced by RAP torch with feed speed as measured by a central thermocouple on a Si wafer .....	<b>Page 60</b>
Figure 5.11 – Plot of temperature induced by RAP torch with feed speed as measured by the outermost thermocouple on a Si wafer .....	<b>Page 60</b>
Figure 5.12 – Plot of temperature on Si wafer with distance from central pass of RAP torch at a feed speed of 4m/min.....	<b>Page 62</b>
Figure 5.13 – Plot of temperature on Si wafer with distance from central pass of RAP torch at a feed speed of 4m/min with a Gaussian fit .....	<b>Page 62</b>
Figure 5.14 – Plot of temperature on Si wafer with distance from central pass of RAP torch at a feed speed of 1m/min.....	<b>Page 63</b>
Figure 5.15 – Plot of temperature on Si wafer with distance from central pass of RAP torch at a feed speed of 1m/min with a Gaussian fit .....	<b>Page 64</b>

## LIST OF TABLES

Table 3.1 – Comparison of modelling integration functions.....	<b>Page 24</b>
Table 3.2 – Sample results for preliminary modelling comparison .....	<b>Page 29</b>
Table 4.1 – Process parameters for experimental investigation of laser heating of ULE substrate using RTD sensors.....	<b>Page 37</b>
Table 4.2 – Process parameters for experimental investigation of laser heating of Trex SiC substrate using RTD sensors.....	<b>Page 37</b>
Table 4.3 – Process parameters for experimental investigation of laser heating of ULE substrate using pyrometers .....	<b>Page 41</b>
Table 4.4 – Process parameters for experimental investigation of laser heating of Trex SiC disc using pyrometers .....	<b>Page 41</b>
Table 4.5 – Process parameters for experimental investigation of laser heating of Trex SiC square using pyrometers .....	<b>Page 41</b>
Table 4.6 – Process parameters for experimental investigation of RAP heating of Si wafer using thermocouples.....	<b>Page 43</b>
Table 5.1 – Experimental (RTD) values and corresponding modelling predictions of laser induced temperature on ULE for sample process parameters.....	<b>Page 51</b>
Table 5.2 – Experimental (RTD) values and corresponding modelling predictions of laser induced temperature on SiC for sample process parameters .....	<b>Page 52</b>
Table 5.3 – Experimental (pyrometer) values and corresponding modelling predictions of laser induced temperature on ULE for sample process parameters .....	<b>Page 56</b>
Table 5.4 – Sample of averaged induced temperature rise on SiC substrates over time for different process conditions .....	<b>Page 58</b>
Table 5.5 – Experimental (pyrometer) values and corresponding modelling predictions of laser induced temperature on SiC for sample process parameters.....	<b>Page 58</b>
Table 5.6 – Symmetry assessment of thermocouple temperatures for RAP torch at feed speed of 1m/min .....	<b>Page 65</b>
Table 5.7 – Symmetry assessment of thermocouple temperatures for RAP torch at feed speed of 4m/min .....	<b>Page 65</b>
Table 5.8 – Experimental (thermocouple) values and corresponding modelling predictions of temperature for RAP processing of Si wafer.....	<b>Page 66</b>

# 1. INTRODUCTION

## 1.1 Context

With funding secured and the go-ahead given for the European Extremely Large Telescope (E-ELT) to begin production, the industry for high quality optics is surely on the rise. The E-ELT, amongst other projects such as the national ignition facility [1], requires nanometre scale surface figure on its optics over large scale components. The E-ELT itself will be made up of 798 [2], each 1.45m across, requiring nanometre surface figure error. This introduces an unprecedented demand for optics and hence the technologies that can produce them at low cost and quickly. There are several existing technologies which are currently in place in terms of surface processing for optics, and these are covered in more detail in the literature review. However, one technology that is of direct relevance is reactive atom plasma (RAP) technology.

The promising RAP technology for dry chemical etching of silicon based optics at atmospheric pressure is a candidate suitable for these uses. It has high removal rates (up to  $0.5\text{mm}^3/\text{s}$  on Corning Ultra Low Expansion glass) [3] and is relatively cheap to operate. This technology slots into a grinding/polishing/RAP process chain which can supply the levels of surface figure error required at high production speeds. This chain of processing is currently being developed in Cranfield and by the company Loxham Precision. RAP is an established technology by itself; however, it is being developed into a new technology.

LAPP is a novel extension of this existing RAP technology. The principle is to include an auxiliary laser energy beam upon the incident area of the plasma plume. This energy beam provides an extra component of the thermal footprint of the tool. Since the chemical reaction that takes place on the substrate surface is temperature dependent the augmented thermal footprint of the tool becomes an augmented etch profile on the substrate. One of the major benefits of this hybrid laser/plasma tool is that it increases overall etch rate by increasing overall temperature. This can be done using a large laser spot size.

As RAP is a process predominantly used for figuring, an additional laser beam also has the potential to increase the base range of functions it can perform. The laser beam, it is hoped, will be able to more accurately figure correct around the edges of substrates, due to the more easily tuneable thermal/etch footprint and greater control over the temperature distribution. It is also anticipated that by using a relatively small laser beam spot size of sub- $400\mu\text{m}$  and as low as  $200\mu\text{m}$  that microstructuring of surfaces could be possible.

## **1.2 Key objectives and reasoning**

- Develop a simulation tool to predict the temperature on the surface of a substrate due to transient incident energy beams.

It can be seen that the thermal aspects of this hybrid system are very important as they define the shape of the tool. Since the technology is so reliant on the temperature of the substrate surface, it follows that a quick method of predicting the thermal properties of a set of process conditions would reduce the time required to characterise the system and save money in processed substrates. This simulation programme could be used for predicting the etch profile of the overall process. Additionally, by monitoring thermal effects in-process, the model could be used as a predictive tool with the ability to feed back into machine control units to maintain etching stability and improve repeatability.

- Design and execute experimental tests to assess the accuracy of the model and determine temperature properties due to energy source.

In order to develop a model with the most accurate results possible, experimental testing is important to assess or verify the predictions. Using thermal sensors of both contact and non-contact variants, the most complete possible picture of the temperature map of the surface can be obtained. The non-contact method selected is pyrometry and the contact methods chosen are RTDs and thermocouples. The testing has the intention of determining the level of confidence that the model can be used to predict the thermal influence of each energy source within the hybrid tool. Additionally, the results will provide their own data toward constructing an understanding of the thermal properties of the system.

- Implement testing of optical material substrates for their response to light of a specific wavelength.

The interaction of laser light with the surface of the substrate is extremely important in determining the energy imparted into the material and hence the temperature to which the substrate surface is elevated. Therefore, it is essential to understand how light of the appropriate wavelength behaves when striking each optical material. Spectrometry tests are designed and implemented using a Fourier transform infrared spectrometer.

## **1.3 Thesis structure**

The structure of this thesis from this point onwards is presented in a standard format on the whole. First, a review of previous literature provides a context for the work. Following this, a chapter on the modelling work is presented with some preliminary results. Then the standard form is followed, with a chapter of experimental equipment and methods preceding results, discussion and conclusions sections.



## **2. LITERATURE REVIEW**

This chapter holds the intention of expressing the ideas and inspiration for the works presented in this thesis. It will provide an overview of the knowledge base from which the thesis was developed and demonstrate the context within which the work is performed. The chapter will be broken down by topic initially. Within each topic, some basic concepts will be presented and general ideas given. This will be followed by more detailed and specific information directly relevant to this thesis.

First, a basic introduction to plasma concepts is given. This is followed by a section on the use of plasmas in surface processing of optics. An account of selected other surface processing methods is the next section, which could be construed as competing technologies. An introduction to laser principles is then given to introduce the auxiliary heat source. Then an assessment of the interaction of a laser beam with plasmas is performed to the level required for this work, and also a review of the interactions of light with solid matter is performed. Following on, an analysis of some literature around the topic of modelling laser heat sources is made, particularly on the mathematical aspects of some papers. Finally a short section is given on surface temperature measurement techniques.

### **2.1 Plasma principles**

In this section, a brief overview plasma will be shown. This includes: what a plasma is, the properties it holds and some examples of its uses.

Plasma can be regarded as a fourth state of matter, possessing unique attributes. The definition of plasma can be expressed as an electrically neutral medium consisting of positively and negatively charged particles [4]. This definition adequately describes the contents of a material in the plasma state but does not provide the full picture. Boyd [5] describes plasma as “any state of matter that contains enough free charged particles for its dynamics to be dominated by electromagnetic forces”, which is somewhat contradictory to the initial statement that plasma is the fourth state of matter but provides key information about the behaviour of the plasma. The dynamics of the matter must be dominated by electromagnetic (EM) forces. This is a fundamental point to consider when attempting to understand or utilise plasma. Boyd also specifies that 0.1% ionised portion of the matter is enough for a material to be referred to as plasma. The main condition that defines whether or not matter is classified as a plasma is the plasma approximation [5].

In this plasma approximation, particles in the matter must be close enough together for particles to interact via EM forces. This means that total number of charge carriers

within the Debye sphere must be greater than 1 (from contributions any number of particles) to provide collective behaviour for the charged particles. The Debye sphere in a plasma has radius of the Debye length given by:

$$\lambda_D = \sqrt{\frac{\epsilon_0 k_B T_e}{n_e q_e^2}} \quad \text{Eq 2.1}$$

Where  $\lambda_D$  is the Debye length,  $\epsilon_0$  is the permittivity of free space,  $k_B$  is the Boltzmann constant,  $q_e$  is the charge of an electron,  $T_e$  is the temperatures of the electrons, and  $n_e$  is the density of electrons.

There are two types of plasma, in broad terms, which may be considered – cosmic plasma and terrestrial plasma. Cosmic plasma considers the naturally occurring plasma in space. There are many types of plasma in space, over vast distances, including intergalactic media, stars of many kinds, solar flares and even just plasma existing in free space. Terrestrial plasma is plasma found on earth or in its atmosphere. This is largely manmade, although lightning is one form of terrestrial plasma that is natural. The range of types and sizes of plasma found on Earth is vast, including everything from magnetic fusion plasma and plasma generated on surfaces by pulsed lasers to the insides of a fluorescent light. [5]

Plasma physics is a vast and complex area of science, and hence it is surplus to the requirements of this work to go into further detail than what has already been covered above. This chapter section was to introduce the concepts behind plasma so the reader has appropriate knowledge of the plasma energy beam's nature.

## **2.2 Surface processing**

### *2.2.1 Atmospheric plasma*

In subsection 2.2.1, a summary will be given of atmospheric plasma processing methods. This technology is reviewed specifically for its use in figuring of optical surfaces such as glasses and semiconductors.

In plasma etching machines, one recognised method of plasma ionisation with a view to etching a surface is to use an Inductively Coupled Plasma (ICP) torch. Inductively coupled plasma uses the principle of induction to excite atoms from a gas into ionised state by electrically stimulating an electron from the outer electron shell of an atom, resulting in an unbound electron and a positively charged ion. A rapidly varying magnetic field is generated by an alternating electric current passing through a coil [6]; the coil is typically several turns of copper in an ICP torch. This rapidly varying current is usually supplied at radio frequency (RF) [7]. A gas is passed through the centre of this coil, whilst being contained so as not to 'short-circuit' the system (for example in a quartz tube), and then increases drastically in temperature and ionises. Thus it becomes

a plasma. As gas is continually supplied through the centre of the coil, the ionised plasma is forced out of the quartz tube. Without the coil to supply current and maintain the ionised state of the plasma, it deionises rapidly after ejection. However, the plasma is present below the base of the torch for appropriate usage: two of the most common applications of ICP torches are plasma etching and spectrochemical analyses. [8]

As an aside, ICP torches are not the only plasma torches – gases can be excited into a plasma state through other energy sources, for example microwaves [9]. However, this is not directly relevant to this project, therefore is not covered in detail.

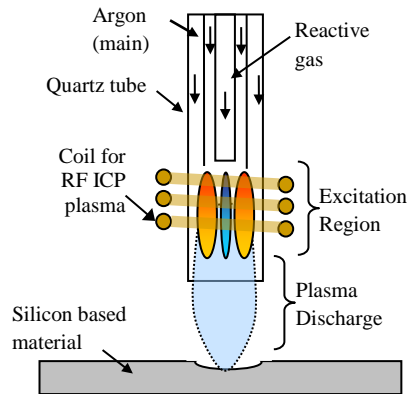


**Figure 2.1: A diagram of an ICP torch. This particular figure is of the RAP300 torch but other ICP torches have similar construction. [10]**

Figure 2.1 [10] demonstrates a schematic diagram of an ICP torch, specifically a design of the torch type being used in the RAP300 machine. Argon flows through both the outer and intermediate tubes: the outer to cool the tube itself and promote a closed conducting loop; the intermediate to generate an argon plasma. Argon is used because it is a Noble gas and therefore inert, having a much lower minimum sustaining power than molecular gases. It is also the most abundant and cheapest Noble gas so for these reasons it usually takes preference. The inner tube contains reactive gas and injects this at appropriate speed to ionise the gas and form a plasma in the excitation region, inside the coil. The plasma discharge is then incident on a substrate upon which a chemical reaction can take place. [7] In the case of etching silicon based substrates, fluorine based gases are often selected as the reactive part, since a fluorine plasma reacts strongly with silicon; these gases include  $\text{SF}_6$ ,  $\text{NF}_3$  and  $\text{CF}_4$ .

The use of plasma to etch or coat materials has been a known technology for over 35 years in some form. An early use was etching of carbon fibres using an oxygen plasma. [11] The current state of torches used for chemical etching provide significant advantages over wet chemical etching – wet etching is isotropic and therefore more difficult to control the etch footprint of, whereas plasma etching is anisotropic so the footprint is easier to maintain in desired shape. [12]

There are two mechanisms involved in plasma etching: sputtering and plasma chemical etching. [13] [14]

- *Sputtering* is the bombardment of the upper layers of a substrate with energised ions to dissociate atoms from the molecular structure of the material. This is a very versatile mechanism in as much as it can be used across a broad range of materials. However, sputtering is difficult to control in terms of small scale refinement of which atoms are bombarded and hence removed from the material.
- *Plasma chemical etching* is neutral chemical reaction between the gaseous molecules and the substrate. This process is selective (it occurs more strongly with some materials than others) and is temperature dependent; the combination of these factors make it much easier to control than sputtering. The temperature dependence is governed by the equation:

$$Etch\ Rate = CN_F\sqrt{T}\exp\left(-\frac{E_A}{RT}\right) \quad \text{Eq 2.2}$$

where  $C$  is a constant to be defined for each material ( $\text{m}^3\cdot\text{s}^{-1}\cdot\text{K}^{1/2}$ ) and  $E_A$  is activation energy ( $\text{kJ}\cdot\text{mol}^{-1}$ ),  $N_F$  is a concentration of fluorine radicals,  $R$  is the molar gas constant ( $= 8.31\ \text{J}\cdot\text{mol}^{-1}\cdot\text{K}^{-1}$ ) and  $T$  is the temperature (K). The Arrhenius section is the prominent dependence in this equation with the  $\sqrt{T}$  factor has a less pronounced effect on the etch rate.

These two different components of the plasma etching process combine in such a way that the combination of the two far surpasses the etch rate achieved by either individually. The sputtering disrupts the surface of the material and this increases surface area on which the chemical reaction can progress. The result is a process which is rapid, selective and significantly less isotropic than wet chemical etching.

Plasma processing has been developed in recent times to process optical materials on micron and nanometre scales. Materials including Fused Silica [15], Silicon Carbide [16], Corning Ultra Low Expansion (ULE) glass [3] and Zerodur [17] have been etched using atmospheric plasma systems. These materials have all been considered for use in optical systems, particularly space optics such as telescopes, due to their good optical performance and high strengths and thermal properties.

There have been various focuses of the work using atmospheric plasma systems for etching. Cranfield University Precision Engineering has been developing their RAP atmospheric plasma system for several years. Work was undertaken by Fanara et al [3] on processing of ULE glass using  $\text{NF}_3$  as the reactive gas. Volumetric removal rates of up to  $0.5\text{mm}^3/\text{s}$  ( $30\text{mm}^3/\text{min}$ ) were demonstrated with up to  $2.8\mu\text{m}$  trench depth when processing straight trenches across ULE samples at  $0.6\text{m}/\text{min}$  feed speed. Since this work by Fanara, further development has been made on RAP processing at Cranfield,

now using SF<sub>6</sub> gas instead of NF<sub>3</sub> and using lower torch powers to preserve torch quartz tube life. Work has been done on fused silica and silicon carbide substrates, demonstrating the adaptability of RAP. Castelli et al [12] have demonstrated the ability of RAP to smooth surfaces down to <18nm RMS using de-convolution algorithms.

The Leibniz Institute of Surface Modification has had a team working on the process which they call plasma jet machining (PJM) [9]. Their work has focussed on modelling of PJM simulations based on thermal and nonlinear processes as well as dwell time to determine the etching rate. Since the technology is being operated at relatively slow speeds and high powers (and therefore high temperatures) [18] these effects are prominent. They have assessed the capability of PJM to process some silicon containing materials but have produced several papers specifically directed at processing Silicon Carbide. They have developed 3 machine heads of different RF powers and sizes to achieve different etching tasks on their optical materials [9]. The work being undertaken by this research group is of some interest, since they concern themselves to a large extent with the thermal effects of their process. Through complex Finite Element Analysis (FEA) simulations they predict very accurately the removal on their substrates and can determine their dwell time algorithm based on these simulations.

While the focus of the Leibniz Institute has been on high power processing of Silicon Carbide, in Japan there has been investigation into Plasma Chemical Vaporization Machining (Plasma CVM) of multiple functional materials, including in particular Fused Silica [15]. The focus was on accuracy and surface defect density [19] during development of Plasma CVM during the 1990s, finding surface roughness of 1.4nm peak-to-valley on silicon wafers and obtaining surface defect density less than 100 times less than that of mechanical polishing. These researchers from Nikon Corporation and Osaka University's Graduate School of Engineering have also focussed on the effects of Plasma CVM on quartz crystals for damage free figure correction. [20]

In Harbin Institute of Technology, China, there has been investigation into an Atmospheric Pressure Plasma Jet (APPJ) machining of Zerodur [17]. The conclusions drawn from this work show that Zerodur, despite being tough to machine using atmospheric plasma methods, is in fact a viable material for processing with the correct plasma parameters. It was seen that material selectivity affected the surface roughness of the processed workpiece, due to the reaction between different layers of the material phases. The reaction progressed fastest on the SiO<sub>2</sub> rich areas. In recent times, this research group has also experimented with what they refer to as a 'contact mode' [21] which uses a charged plate beneath the substrate to improve etch rates by attracting ions towards the substrate. This new method is currently undergoing characterisation.

### 2.2.2 *Other surface processing methods*

This subsection will provide a brief review of some other methods of processing surfaces. In terms of optical surface processing, aside from the atmospheric plasma methods mentioned above two other technologies are covered: magnetorheological finishing and focussed ion beam (FIB) machining. An outline of some of the industrial uses of lasers in material processing is also covered.

Magnetorheological (MR) methods are based on the principle of ferromagnetic liquids that increase in viscosity under the influence of a magnetic field. In general, a rotating wheel is surrounded by a 'ribbon' of MR fluid comprising of a carbonyl iron portion which responds to the magnetic field and a carrier fluid which contains nonmagnetic polishing abrasives. The material removal mechanism is dominated by shear stress forces not force components normal to the substrate surface. This leads to minimal damage below the workpiece surface and very little stress deformation within the workpiece, much less than compared with traditional mechanical polishing. [22]

One particular institute who specialise in the use of MR finishing is QED technologies. They have demonstrated a removal footprint following a characteristic shape. This characteristic shape is specified by the tool, meaning that the tool footprint cannot be altered in shape during the process. However it can be altered in size by varying the thickness of the fluid ribbon. They claim removal rates of  $0.75\text{mm}^3/\text{min}$  on materials such as Fused Silica, resulting in a surface roughness of  $1\text{nm}$  [23; 24]. The low material removal rate means that processing substrates of sizes comparable to those being processed by RAP takes hundreds of hours of process time. This means the process is comparatively inefficient and expensive. However, the surface quality is extremely good.

Ion beam methods of surface figuring develop the idea of sputtering material from a surface through bombardment with ions. In a vacuum environment, ions with energy of  $\approx 1\text{keV}$  are generated and controlled onto a surface using an electrostatic field [25]. The ions disrupt the surface structure if the ion energy is above the bonding energy of the substrate material and when the bonds are overcome some material is removed from the surface. The probability of the bonding energy being overcome decreases with distance from the centre of the beam following a Gaussian function, giving a Gaussian removal function for focussed ion beams.

In a manner similar to RAP processing mentioned above, the program for figuring a surface is a rastering pattern, using the Gaussian profile in a dwell-time method. The length of time the beam stays over an area determines how much material is removed. [26] The pattern for processing is determined using a de-convolution algorithm to translate amount of material to be moved into amount of time required over one area (or equivalently how rapidly the ion beam passes over each area and how many times). Typically, argon ions are selected.

Variants of ion beam methods have been developed claiming different process conditions and capabilities. Spatial resolutions have been claimed resulting in minimum spot sizes of between 75-1000 $\mu\text{m}$  full width at half maximum (FWHM), with up to 15mm FWHM achievable. Material removal rates of up to 150mm<sup>3</sup>/hr (2.5mm<sup>3</sup>/min) have been claimed on BK7 glass. The surface roughness and peak-to-valley have been claimed variously down to approximately 3nm root mean square (RMS) using several iterations and the peak-to-valley has been reduced by a power of ten for figuring of surfaces such as fused silica. [25; 26]

Benefits of ion beam figuring are its highly deterministic nature, the absence of subsurface damage and the tuneable tool footprint. Disadvantages are its fairly slow removal rate, the expense of running and the requirement of vacuum chamber to operate.

Lasers are also used to process surfaces [27], although not as predominantly for glass as for metals, organic and synthetic materials, and semiconductors. The reason for this is that glasses are often intended for use in reflecting or transmitting/guiding light, meaning they are utilised so as not to absorb light. This means that the laser, which relies on light entirely for its interaction with the surface, is hampered in this aspect. Laser surface interactions generally fall into 2 categories – continuous wave and pulsed – like lasers themselves.

Continuous laser processing involves the transfer of heat via radiation (light) and raising the temperature of the surface in a known area. This can be used for annealing, cutting and welding amongst many other uses. [28] Pulsed laser operation results in a very different surface reaction. The energy is transferred to the surface in a very short period of time (of the order of nanoseconds or less, depending on the operation of the particular laser), resulting in superheating of very small areas, causing instantaneous evaporation of material or generation of plasma from that material. This material is ejected with force from the surface and is thus removed. [29]

Clearly the aforementioned surface processing methods have their own benefits and positives as well as disadvantages. Some of them could be used in conjunction with RAP; others instead if one were to consider a process chain. However, with LAPP involving two already existing surface processing technologies and combining them into once hybrid tool, it is hoped that this will become one of the standout technologies in the field. The laser, of course, is the key component which increases tuneability and capabilities of the already existing RAP technology. While the laser has been mentioned in this section as a tool for surface processing, their operational principles have not been properly introduced. This brings us nicely into the following section, a review of the topic of lasers.

## 2.3 Lasers

This section aims to outline the basic physical and operating principles of lasers. Following some introductory comments and physical points, a subsection will introduce laser interactions with material in the plasma state. Subsequently, a view will be given of the interaction of light with solid matter, in particular absorption of light. Finally, and perhaps most importantly for the purposes of this thesis, the mathematics behind modelling of laser heat sources will be studied and the literary precedence for laser models will be examined.

Lasers, so called from the acronym Light Amplification by Stimulated Emission of Radiation, are a relatively young phenomenon in terms of physics – having only been around for approximately 60 years. The acronym pertains to the specific process involved in increasing the intensity of light – stimulated emission. When light interacts with a medium, there are two main processes that can occur, optical stimulation and stimulated emission. Optical stimulation is by far the more common of the two processes. It is the case where a photon is absorbed by the medium, transferring its energy to an electron which becomes excited. This electron may naturally return to its ground state and emit another photon, but these are common natural processes. [30]

The more interesting case to study is when a photon passes through a medium and its electric field interacts with that of an already excited electron. This interaction causes the excited electron to move to a lower energy state with an energy drop equivalent to the photon energy, and emit another photon of the exact same energy as the stimulating photon. The inherent physics of this process means that each further photon that arises by stimulated emission has the same phase, same direction and same wavelength as other photons.

This can lead to incredibly bright light which can be focussed down to a tiny spot with very low divergence. With selection of the correct optical medium and stimulating photons, the laser can be tuned to a variety of wavelengths depending on the bandgap of the material. Specific materials have electrons that can only be stimulated to and from set energy levels related to the chemical composition of that material. For example, CO<sub>2</sub> lasers operate primarily at 10.6μm because (using  $E = h \times f$  to relate energy to frequency using Planck's constant) the energy levels within CO<sub>2</sub> molecules are at such a distance apart (in an energy domain) that when stimulated emission occurs the radiation has that wavelength.

Since the light emitted is electromagnetic radiation it can be considered as a method of energy transfer. [29] The intensity of this radiation is (usually in the case of a laser as a tool) extremely high, resulting in a large amount of energy transferred. The energy conveyed by a laser is usually given in Watts, or Joules per second, when referring to a continuous wave laser and in Joules when discussing pulsed lasers. The reason for this is that when a laser is operating continuously, the amount of energy transferred over a



period of time is usually required. Conversely, pulsed lasers are usually used for very short time periods, so the amount of energy transferred in each pulse is the information desired since this is what will be determining the result of the laser pulse. Various distributions of the energy through the cross-section of the beam are possible, but the basic operating mode of a laser is usually that to produce an imperfect Gaussian profile – with more energy in the wings of the profile depending on the quality of the laser, a factor determined by its construction. Other common intensity/energy distributions are ‘flat-top’ profiles which have uniform temperature, and ‘donut’ profiles, which are shown in Figure 2.2. [31]

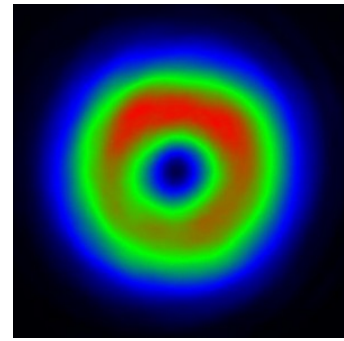


Figure 2.2: Image of a laser donut intensity distribution. [31]

### 2.3.1 Laser-plasma interactions

When considering Laser Assisted Plasma Processing, it must be noted that whilst the two individual energy beams are interacting with the substrate they are also occupying the same volume of space for a period of time before they strike this surface. Laser light interacts with any matter that is not *entirely* transparent at the wavelength of that laser. Thus, any material that is opaque to an extent (almost all materials) will have an interaction with the laser. Since the plasma plume, although it is being considered as an energy beam for the purposes of surface processing, is fundamentally a form of matter, the interactions of the plasma itself with the laser light must be considered.

Plasma interactions with lasers has been extensively documented. While not exclusively so, a large proportion of the work produced on the subject is in reference to pulsed lasers operating with very short pulse times. [32] When these timescales are considered, the focus is on the evaporation and ionisation of material ejected from the surface of the substrate. Since ultrafast lasers impart so much energy onto the substrate, the material is converted to a plasma over an incredibly short timescale, which interacts again with subsequent laser pulses, interfering with the quality of the laser surface processing. As this is a prevalent issue in laser machining, this has been widely studied. However, dependent on the material being processed, the plasma generated is typically localised and very dense. This is not directly applicable for several reasons:

- *Direction of plasma motion.* The plasma in the case of RAP processing is being ejected from a torch **onto** the substrate surface, whereas in the aforementioned case the plasma is ejected **from** the substrate surface.
- *Volume occupied by plasma.* The localised plasma within the laser beam that is generated by ultrafast lasers is much smaller in volume than the plasma plume from a RAP torch which will be orders of magnitude larger.

- *Plasma electron density.* The electron density of the plasma determines the amount of electrons/ions that will interact with the laser and thus the change in the properties of each energy source due to the other. RAP plasma is much less dense than that generated by pulsed laser machining.
- *Laser wavelength.* The laser wavelength determines its interaction with the plasma. Ultrafast/pulsed lasers often have much shorter wavelengths than the CO<sub>2</sub> laser being selected for LAPP.

However, despite not being directly applicable, many of the same theoretical concepts are relevant and useful in considering laser interactions with plasma in the context of LAPP.

A key factor in radiation interacting with plasma is the absorption and reflection of the light from the matter (plasma) as is the case with any light interaction with matter. The reaction of plasma when stimulated by radiation is dominated by plasma oscillations. These occur when the frequency of the radiation in question is at or above the plasma frequency. This plasma frequency is given by equation 2.3 with  $\omega_p$  the plasma frequency,  $v_e$  the thermal electron velocity,  $\lambda_D$  the Debye wavelength,  $n_e$  the electron density and  $m$  the electronic mass.

$$\omega_p = \frac{v_e}{\lambda_D} = \sqrt{\frac{e^2 n_e}{\epsilon_0 m}} \quad \text{Eq 2.3}$$

When  $\omega_p = \omega$  then  $n_e = n_{crit}$ : the critical electron density. The critical electron density thus determines the interaction of the light with the plasma. [10] This is dependent on the wavelength/frequency of the light being considered, and thus a relation between electron density and wavelength can be plotted. [29]

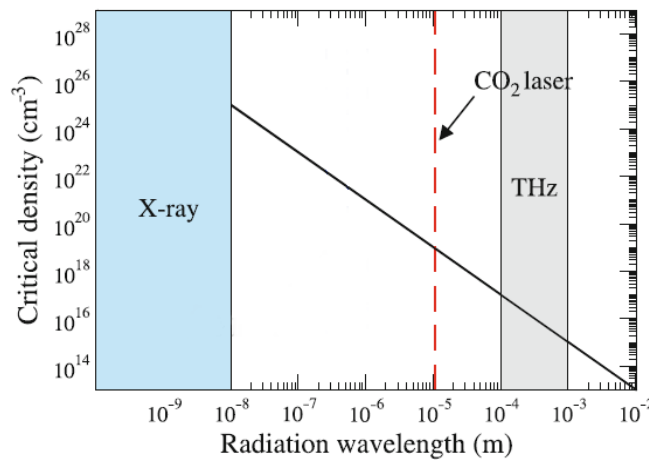


**Figure 2.3:** Plot of critical electron density with radiation wavelength, with indication of CO<sub>2</sub> laser wavelength in red dashed line. The solid black line is the line below which the interactions are negligible. [29]

As can be determined from Figure 2.3, for a specific wavelength a critical electron density can be identified. If the electron density in a plasma is below this value for the

wavelength of the incident light then the plasma oscillation interactions with the laser become minimal. This is because for a higher frequency (shorter wavelength) of light than the plasma frequency the plasma is transparent as the electrons cannot oscillate rapidly enough in response to the light and no resonance occurs.

The other main effect is the refraction of light as it passes through the turbulent gaseous region inhabited by the plasma. This is a phenomenon not specific to the fact that the material is in a plasma state, it would occur with any fluid flowing in a turbulent manner. The refraction changes as the gas has an inhomogeneous refractive index depending on its density and particular chemical makeup at each spatial co-ordinate. This can introduce some lensing effects in a laser light, defocussing the laser (if it is focussed on the plasma area) or marginally altering the direction of laser propagation. The science behind these interactions delves into the complexities of fluid dynamics [33] and thus is not included in more detail in this thesis.

### *2.3.2 Light-solid matter interactions*

This subsection will focus on the interaction of the light from a laser with solid matter. This has the specific view to examining the boundaries between air/free space and a solid object, and the behaviour of light as it strikes this boundary. The effects of opacity on light propagating through the solid matter will be reviewed also. These aspects are very important when considering the processing of a material, in particular when using a laser since the laser beam is a very intense column of light that could cause serious injury if misdirected. The contents of this subsection draw mainly from the textbook by Weiner and Ho [34].

When light interacts with a boundary, the result is a portion of that light being reflected and a portion being transmitted through the boundary into the material. The relation is determined by a collection of different factors - these include the angle of the incident radiation, the polarisation of the light, the surface roughness and the wavelength of the radiation amongst others. For the purposes of this project, the dependence of reflection on wavelength need not be further considered seeing as the wavelength of the laser within the LAPP system is fixed at  $10.6\mu\text{m}$  so this will not be a variable within the experimentation.

The variation of the absorption/reflection with the incident angle, polarisation and surface roughness are to an extent linked to one another. Light polarised in different planes has a different interaction with a surface due to the direction of the electromagnetic oscillations relative to the plane of the surface. To account for this effect, Brewster's angle has been implemented within the LAPP machine, which is the angle at which one polarisation of light is entirely absorbed. This minimises the different reflectivities at different polarisation issues. However, the angle of incidence at

which this Brewster's effect comes into consideration has its own reflectivity at the selected wavelength. The percentage of light reflected at this angle must be measured and taken into account.

The surface roughness relates to the reflectivity based on two main factors: the varying angle of the surface relative to the light's propagation with the roughness variation and the potential for multiple reflections. If the light can enter the 'troughs' of the undulating surface then there is potential for multiple reflections, allowing the radiation to strike the surface multiple times, with a portion being absorbed each time. Therefore, to an extent a rougher surface increases absorption on optical scales. The varying angles the surface presents when rougher can lead to reflections with either higher or lower reflectivity depending on the new angle of incidence. The combination of the above factors means that roughness of surface will affect laser interactions with a tendency to increase absorption with roughness.

Once the boundary interaction has been dealt with, the light is absorbed by the material as it propagates along its path. The rate of absorption of the radiative energy by the material is dependent on a factor known in some fields as the opacity. This can be explained by the amount of light absorbed with propagation distance. The penetration depth is the distance at which the intensity of radiation has dropped to  $1/e$  of its surface value, which results in the power dropping to  $1/e^2$  of its surface value. The surface value to which the reference is made is actually taking into account that a portion of the radiation from an incident beam would have already been reflected. So, for the portion of the radiation that is transmitted across the boundary, the penetration depth is given by equation 2.4.

$$\delta_p = \frac{1}{\alpha} \quad \text{Eq 2.4}$$

Where  $\alpha$  is the absorption coefficient, the scaling factor in the Beer-Lambert law for decrease in radiation intensity, shown in equation 2.5.

$$I_z = I_0 e^{-\alpha z} \quad \text{Eq 2.5}$$

$I_z$  is the intensity with distance,  $I_0$  the initially intensity, and  $z$  the displacement along the axis of electromagnetic propagation. The absorption coefficient is dependent on wavelength of light and the specific material through which the radiation is propagating. Specifically in infrared wavelengths, at which the primary mechanism of absorption is motion of molecules and atoms in the form of heat, the absorption coefficient is strongly dependent on the relation between the wavelength of the radiation and the length of the molecular bond. If the vibrational frequencies of the constituents of the material are equivalent or near to the wavelength of the radiation, the vibrations in the material will be stimulated and the radiation absorbed. The proportion of the radiation transferred to these oscillations is what determines the absorption coefficient.

### 2.3.3 Mathematical Modelling

The mathematics behind modelling the transfer from heat of a laser, like many other aspects of mathematics, is a reapplication of well-known ideas. The conduction of heat through various media has been known mathematically for a long time, and was compiled in the book by Carslaw and Jaeger in 1946, then in a second edition featuring additional mathematics in 1959. The mathematics of heat transfer to a surface as a point source was proposed in this book, which was then taken further by early laser modelling papers by Lax [35] [36] as well as Cline and Anthony (C&A) [37]. Both of these papers were in press at the same time in 1977, and do not reference one another, therefore it is expected that similar work was conducted separately and this is not a case of plagiarism.

The basic principle that both papers follow is modelling of Gaussian sources by the superposition of multiple point heat sources following a Gaussian intensity distribution over known distance across the surface (the beam spot diameter). The papers both concern themselves with the transient analysis condition as this was particularly common as a use of lasers at the time. Since the maths involved in both papers is very similar, of the two just the C&A paper will be described from this point onwards.

The solution to a temperature rise can be found by solving the diffusion equation of heat within the material, equation 2.4.

$$\frac{\partial T}{\partial t} - D\nabla^2 T = Q/C_p \quad \text{Eq 2.4}$$

The surface intensity distribution, a circular Gaussian distribution, is normalised to give a total power  $P$  and spot radius  $R$ . Then a heat flux can be written in terms of these two factors, an exponential term relating to the Gaussian distribution and a depth function. This equation, in Cline and Anthony, is expressed in equation 2.5. The depth function is used to ensure that below the level where the laser absorbed the equation to describe the temperature is continuous and above this level it is zero, with  $\lambda$  the absorption depth.

$$Q = \frac{Pe^{[-[(x-vt)^2+y^2](2R^2)^{-1}]}h(z)}{2\pi R^2 \lambda} \quad \text{Eq 2.5}$$

Using a Green's function method of obtaining a solution for the diffusion equation, we can find the temperature at coordinates  $x, y, z, t$  within the material from the influence of the source at surface point  $x', y', t'$  in space and time, where  $t$  is later than  $t'$ . The Green's function is multiplied by the surface source distribution and integrated with respect to  $x', y', z', t'$ . The spatial integrals are known results, so the temperature is given by equation 2.6. This cannot be integrated analytically, so is numerically solved instead for specific values.

$$T = \frac{P}{C_p} \times \int_0^\infty \frac{e^{[-\{[(x+vt')^2+y^2](2R^2+4Dt')^{-1} + (z^2)(4Dt')^{-1}\}]} }{(\pi^3 Dt')^{\frac{1}{2}}(2R^2+4Dt')} dt' \quad \text{Eq 2.6}$$

At this point a Kirchoff transformation is conducted. This is of the form of equation 2.7 and means that the calculation of temperature can account for temperature dependence of material properties – in particular the thermal conductivity. This transformation for linear temperature to real temperature completes the solution of the diffusion equation for temperature locally.

$$\theta(T) = \int_{T_0}^T \frac{K(T)}{K_0} dT \quad \text{Eq 2.7}$$

The paper by Nissim et al [38] takes a further step from the C&A paper in solving the problem for an elliptical beam spot. This is more useful as in a real situation it is unlikely that a laser beam spot will ever be 100% circular. For this reason the Nissim model is the one that has been chosen, with contributions from both the C&A and Lax models.

Since these fundamental papers on analytically modelling the solution to laser heat transfer to a surface, there has been extensive study on using computer methods to further develop these ideas. A large portion of the work, conducted by Manca et al [39; 40] and Loza et al [41], was conducted using finite element methods.

The finite element solutions to the problem are more specific to individual problems. The solution is generated by stating the thermal conductive problem and setting particular boundary conditions and initial conditions with respect to the heat source and the workpiece. By modelling the workpiece as an amalgamation of small elements, each connected and interacting with neighbouring elements the solution can be generated numerically. This method has its advantages, including very good accuracy and being able to specify variation of material properties, along with representing a real and physical solution. However, finite element analysis is very consuming of time and computer resources.

Other papers like that by Loze and Wright [42] take ideas put forward by Carslaw and Jaeger and use them in a more applied context. That paper discusses the laser absorption by multiple layered materials analytically. This is less useful for LAP applications as in terms of the substrate size with respect to the laser spot, the substrate can be considered semi-infinite and homogeneous.

Aoyagi and Lu [43] have developed a paper on temperature rise from a doubly Gaussian intensity profile. This may be a particularly useful paper in as much as it may be used to predict the temperature induced on a surface by LAP processing. The RAP torch may be modelled as a larger Gaussian heat source and the laser as a smaller one. By modelling, in a similar way to that suggested by Aoyagi and Lu, both sources together, a combined analytical model for the LAP process may be developed.

Lu et al (the same Lu as mentioned above) have produced work [44] on laser light incident on/in Gaussian shaped holes, similar to those found in the form of trenches

from RAP processing. By modelling the heat source as a superposition of two components (one from the surface of the hole, and one by a mirror image about the  $z=0$  plane) the temperature rise in the hole can be modelled. It is shown that the peak temperature depends strongly on hole depth and weakly on hole radius. This may be possibly to incorporate if LAP experimental results do not correlate strongly with the predicted temperature rise from a flat surface model.

## **2.4 Temperature measurement**

This section describes which devices have been selected for measurement of the temperatures to be investigated in this thesis. A working principle of each is given and the reasons it was selected rather than an alternative. The temperature measurement devices covered are: resistance temperature detectors (RTDs), thermocouples, pyrometers and thermal imaging cameras.

RTDs operate on the principle that a conductive material, most commonly a metal, has varying resistance with temperature. As the temperature in a metal increases, the lattice structure of the material vibrates more vigorously. These vibrations (quantised in phonons) interact with electrons attempting to pass through the material and cause them to experience more difficulty doing so – i.e. resistance. The resistance can be measured and equated to a relative temperature, as the relationship is often linear in metals, particularly at high temperature. A common RTD material is platinum, and the RTDs are specified as Pt100, meaning that they have resistance of  $100\Omega$  at  $0^\circ\text{C}$  temperature. From this temperature upwards they have higher resistance and downwards they have lower resistance. Using a data logger or data acquisition device these sensors can be calibrated so that the acquisition of the resistance of the wire is converted into a corresponding temperature. They are a contact method of temperature measurement so one can know exactly where the temperature being measured is located. They have a low thermal mass and can easily be found in small sensor heads. [45]

Thermocouples, whilst being generally considered as a less accurate contact method of temperature measurement than RTD sensors, have their own benefits. Since they are cheaper they tend to be a more financially viable solution for contact measurements in instances where sensors or substrates are expendable. On substrates used for thermal characterisation, such as silicon wafers, thermocouples are preferable to RTDs since once the sensor has been stuck it cannot be taken off non-destructively. The sensors are still accurate enough for the experiments to be conducted in the plasma chamber as they can still measure to sub-degree levels. [46]

A pyrometer is a non-contact method of measuring temperatures. It is based on the detection of emitted radiation within a field of view. A pyrometer measures the radiation from whatever is within its field of view, and the field of view is determined

by optics specified when the pyrometer is purchased. The material being measured with the pyrometer should have a known emissivity, either temperature dependent or approximated in the temperature range being measured. The emissivity determines what proportion of the temperature on the material's surface is emitted as radiation. The material emits radiation as a fraction of that of a black body following the relation  $Q = \varepsilon \sigma T^4$  where the radiated heat is related to the fourth power of the temperature by multiplication by the emissivity and the Stefan-Boltzmann constant. The pyrometer detects the radiated heat and uses this equation to calculate the temperature of the object within its field of view. A pyrometer is chosen to measure temperature in this case because of its non-contact nature and relatively low cost. The accuracy of a pyrometer is one of its disadvantages, along with its slow response time – these both suffer on less expensive models, but for a reasonable measurement of temperature integrated over the field of view, the pyrometer is a useful tool. [47]

Thermal cameras are an expensive technology in general, but provide a good resolution of temperature over their field of view. They are a non-contact method of temperature measurement, similar to pyrometers but they resolve temperature at many different points across an image depending on the intensity of infrared radiation being received. They tend to not discriminate between different wavelengths of infrared radiation, which could be considered a disadvantage. They also have fairly slow response time if used as a video camera. However, for taking a snapshot of temperature during a specific process they provide useful qualitative information about what temperature can be detected at particular points within the camera's field of view. This can be useful in determining whether the other temperature measurement devices are having an influence upon the temperature of a process. [48]



### 3. MODELLING

The intention of this chapter is to present the development of the model to be used for predictive purposes in the LAPP project. The purpose of the modelling work is to provide a tool to predict the thermal effects of laser assisted plasma processing. This has the primary objective of simulating the surface temperature induced by the laser energy source, both in distribution and magnitude. These results can be used for reduction of the number of physical processes required to characterise the LAPP system by eliminating those experimental runs which would be outside the acceptable range. This will result in overall cost reduction due to reduced number of surfaces required. Another intended use of the model is to provide information for a real-time feedback loop to be included in the LAPP system.

The two types of models initially considered for this application were finite element methods and analytical methods. The analytical method under investigation involves the solution of fundamental equations mathematically for specific cases, making a number of assumptions along the way. A finite element method is generally considered the more accurate model overall by dividing the problem into multiple smaller blocks and examining the interaction of these blocks. A finite element simulation tends to account more completely for the physical aspects specific to the problem such as the substrate dimensions. However, in order to achieve the improved accuracy over the analytical model, a finite element model sacrifices speed.

A thought about the calculations involved in each model type (which are conducted by a computer in modern times) is necessary. A finite element solution is basic on determining temperature at every point specified within a substrate from a generic equation. The solution must be built from every loaded node taking into account properties from each node separately based on neighbouring nodes. The result is a very high number of calculations required, which has a significant demand on computing resources. Conversely, analytically modelling the problem can mean a single equation can be solved for each desired point. The work is done in hand-solving the differential equation beforehand for a specific source, resulting in rapid computation later. The amount of solutions generated is directly correlated to the amount of points being inspected (and hence resolution of the temperature map of the substrate) which can be increased or decreased to fit the solution density required. This means that the analytical type of model is much quicker than finite element simulation in general.

### 3.1 Analytical model

In the case of LAPP, the analytical approach is selected. When weighing up the benefits and drawbacks of FEA in comparison with those of an analytical model, the applications for the model must be assessed. Each individual experimental pass within the LAPP machine can take up to 36s depending on travel speed and substrate size, so if modelling is taking a long time compared with this (i.e. tens of minutes upwards) then the suitability of the model for use in determining process effects is called into question. A previous modelling investigation conducted into a Gaussian heat source within Cranfield University Precision Engineering Institute was implemented using FEA to model a RAP torch and achieved degree-level accuracy but took tens of hours to run. On this evidence, the analytical model was preferred. Another factor that influenced this decision was that the degree of accuracy given using FEA is not required as this level of temperature control would influence LAPP to a scale below that which is currently measureable within the Institute. Therefore, the extra accuracy given by the FEA would be a surplus to necessity.

#### 3.1.1 Programming detail

A single numerical integration is the basis of the code written to perform the modelling. The equation for which the integration is performed is taken from the literature (see section 2.3.3). The integral function selected in Matlab is 'quadgk'. This function is a numerical integration between two specified values using Gauss-Kronrod quadrature, an approximation to an integration using a weighting system. There was little noticeable discrepancy between solutions generated using other numerical integration functions, as can be seen in Table 3.1.

**Table 3.1: Three types of quadrature available as Matlab functions for numerical integration and the temperatures predicted for an arbitrary scenario of Gaussian surface source heating of a substrate.**

Quadrature	Gauss-Kronrod	Lobatto	Adaptive Simpson
Temperature (°C)	327.9172	327.9172	327.9172

The usually variable process parameters in the above example are kept constant, and it is just the integration that is changed, so the parameters become arbitrary. The results hold to 4 decimal places consistently for the numerical integration of this equation – in excess of that required by the system. Another factor in this case would be the processing time required to perform the calculations. However, an investigation into the modelling using each quadrature showed no appreciable difference in the calculation times between each set of quadrature, therefore the default setting was used.

The implementation of the transform within the code requires a brief explanation. Once a linear temperature has been established through the aforementioned numerical integration, the output from this function is converted via a Kirchoff transformation into a 'real' temperature. This implements a function, which will be detailed later in the document, taking into account the temperature dependence of material properties and the initial temperature. This allows for improved accuracy and also better clarity in the temperature output as it is now in a format where it is a real observable temperature.

One of the advantages of using an analytical model is that it is straightforward to specify a range of calculations that are to be made. By writing a separate code to generate a range of inputs for the integration, a customisable output can be generated. This means that the density of the mesh of solutions can be refined to specification and the area/volume being solved for can be varied in size and location. The specific comparisons to be made are those with pyrometer fields of view both at  $45^\circ$  and normal to the surface, and with RTD sensors; all these can be at varying distances from the centre of the laser spot but are all surface areas. These comparisons require elliptical, circular and square output matrices respectively for their integrations to be written into. The elliptical outputs are made by generating rectangles of results of the axes of the ellipse, then masking out the corners to leave an elliptical shape of results. A similar process is conducted for circular outputs. The square outputs are generated simply using a square matrix.

### *3.1.2 Starting assumptions*

As with any predictive tool, some assumptions have to be made and acknowledged in the generation of simulated temperature values for an analytical model. The assumptions made will have an effect on the accuracy of the results when compared with real temperature. The assumptions put forward within this chapter are justified and reasoned individually.

An assumption that must be made is one of surface emissivity and absorbance and the temperature dependence thereof. The absorption is likely to vary with temperature. However, with current equipment it is not possible to measure this dependence for the optical materials being investigated. These are also not dependences that have been measured by the manufacturers of the materials so are unknown quantities. The above situation regarding temperature dependences is also applicable to the emissivity. For these reasons, the documented (in the case of emissivity) and measured (in the case of absorbance) values have been taken for both materials at room temperature. The room temperature values will not be true for higher temperatures, it is fair to assume, although it is presently not possible to explicitly express how different the values will be.

The models selected to develop from literature are concerned with laser beams perpendicular to the substrate surface being analysed. This is not the case within the scenario which we are modelling, in which the laser beam is incident at 65°. To account for this discrepancy, an elliptical beam spot is being modelled as perpendicular to the surface. Although this is not the case in real life, it accounts for the spot skew due to the angle. The penetration of the laser beam into the substrate would be an issue when equating the perpendicular beam to the 65° beam in some models, however in this instance the model is of a ‘surface’ source. Although this is difficult to define in a physical sense (i.e. where does the ‘surface’ begin/end in terms of atoms) it means mathematically that the heat source is a two dimensional source which simplifies the calculations. This factor, along with negating the effects of equating angled and normal laser sources, means it is a fairly elegant option.

An interesting point which must be noted and is fundamental to the accuracy of this modelling is a discrepancy in nomenclature between the mathematician’s expression for the radius of the beam and that of the modern laser engineer. Since the mathematical approach to this modelling is based on a Gaussian function, it has a classical Gaussian approach to defining the size of the source. This is expressed as a radius of  $\sigma$ , the standard deviation of the function. This represents the distance from beam centre at which 68.2% of the beam’s energy would be enclosed. Conversely, the common engineering term when describing the size of a laser beam is  $1/e^2$ , representing the value where the energy of the beam falls to that proportion of the maximum value, which results in 86% of the beam’s power being enclosed. Therefore, it is necessary to utilise a conversion factor to gain continuity between radii for comparisons between modelling and experimental work. The values of radii used in experimental work are taken as the easiest to work with as other parties will be interested in the data in this format. This has led to a conversion factor of 0.793 being applied to values of radii (within the program) to change the experimental values input into the correct form.

### 3.1.3 Transformation

The transform referred to is essentially a conversion between the calculated linear temperature that the equation generates and a ‘real’ temperature which accounts for the temperature dependence of thermal conductivity. The linear temperature is that which would be observed on a surface when analysing a material with no temperature dependence of thermal conductivity. On silicon based materials this has the potential to be a very important factor, given that the behaviour of silicon with temperature is so changeable depending on the structure of each individual molecular structure.

The conversion is mathematically known as a Kirchoff transformation, and the new variable to which the linear temperature is converted is described by the relation shown in equation 2.7. Various literature sources (reviewed in chapter section 2.3.3) have

differing implementations of the transformation. However, the approach taken in this instance is based on a mathematical derivation and an approximated thermal conductivity function from material properties data sheets. The derived form allows for input of a dependence of the thermal conductivity with temperature as an equation and is calculated through from equation 2.7. The empirical part of the method requires input of a set of data points from existing data on thermal conductivity which are then plotted and curve fitted. Once the curve has been fitted, the equation can be observed and this can be implemented to transform results.

The data is not currently available for thermal conductivity with temperature for the specific optical materials being investigated. Therefore the empirical approach for ULE can only be approximated by known dependence of similar materials – silicate glass for example. This will, however, give an indication of the thermal conductivity dependence of a glass on temperature and help to identify the trend. Should material data become available in the future this approach could be implemented to a much more accurate degree and thus become the more reliable of the two methods. Due to the unknown dependence in SiC, this has been taken in this case as constant. A request was made to the suppliers of the material but they were unwilling to supply substrates for testing or provide specific data.

#### *3.1.4 Preliminary assessment*

As an initial assessment of the code's functionality, results obtained experimentally prior to the involvement of the writer in the project were compared with equivalent simulated temperatures. This provided an indication of how accurate the predictive tool is in its raw form to match data from an 'uncontrolled' environment – in other words an environment not specifically designed for model verification.

The experimental results in question were designed to match the laser configuration of an original, early LAPP machine. The system had been designed to incorporate a laser into the RAP300 machine without replacement of any major parts. This involved the propagation of a laser beam via two reflecting mirrors which resulted in a 65° angle of incidence of the laser beam. This configuration was emulated as can be seen in Figure 3.1, the red dashed line indicating the laser path. The pyrometer stand-off distance was 20mm, resulting in a 7mm field of view.

The laser used was a higher powered laser than in the aforementioned early LAPP system – a 200W CO<sub>2</sub> Rofin DC010 laser operating at 10.6µm. However, due to the variable power input this could be reduced depending on the required temperature rise. The process conditions had been selected based on existing RAP process conditions with laser power varied to meet target surface temperatures on each material exceeding

300°C. The beam spot, due to lack of focussing optical components was elliptical with 24.3mm major axis after being skewed by the incidence angle.

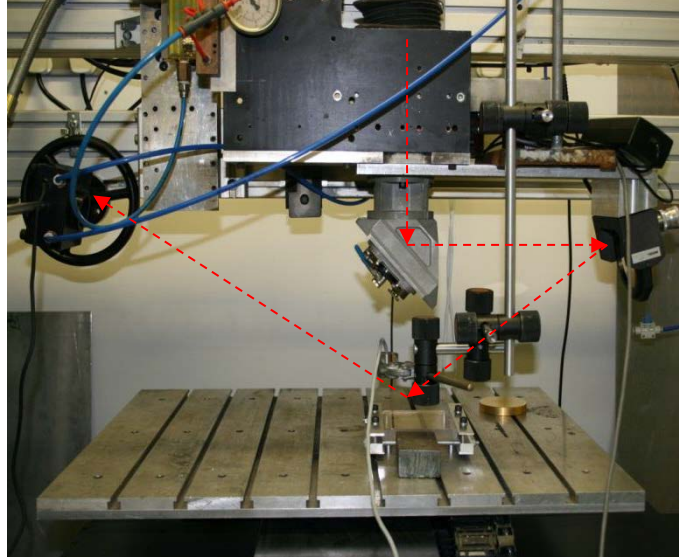


**Figure 3.1:** Experimental configuration of early work to determine temperature rise on optical materials due to incident CO<sub>2</sub> laser beam. The optical configuration consists of the Rofin DC010 laser, a 90° reflecting mirror, and an angled mirror at 25° to the incoming beam. The beam then strikes the substrate at 65°, with any reflected laser radiation being measured with a power meter. The temperature rise on the substrate surface is measured using an infrared pyrometer positioned normally to the laser striking zone. The substrate is moved using a CNC controlled stage.

Some of the process parameters can be seen in Table 3.2 along with sample peak temperatures and a modelling prediction. These temperatures have confidence levels based on the variation in observed temperature due to surface quality variation. The inconsistent surface finish on the substrates used for the work meant a slight inhomogeneity in absorbed laser light; therefore the values taken are mean values for the time at which the temperature rise is observed. Since the surface roughness of the samples used for this work is not available to the writer it has not been possible to locally account for the varying absorption.

**Table 3.2: Sample process conditions for some preliminary investigation into modelling. The confidence bounds of the pyrometer values are based on fluctuations around the stable temperature due to surface quality variation locally.**

Material	Power (W)	Feed speed (m/min)	Model result (°C)	Pyrometer reading (°C)
ULE $\epsilon=0.848$	248	3	404	$523\pm12$
	248	4	396	$428\pm10$
SiC $\epsilon\sim0.95$	244	3	388	$365\pm7$
	244	4	383	$364\pm7$

To match the measured data with modelled simulations the correct adaptation of the model was determined. The correct regions of ‘points’ which form the temperature map calculated by the model had to be ascertained and programmed to match the pyrometer field of view. The simplest way to do this for a perpendicular pyrometer was to generate a full square of results and mask out the corners using ‘Not a Number’ values. An example of this can be seen in Figure 3.2.

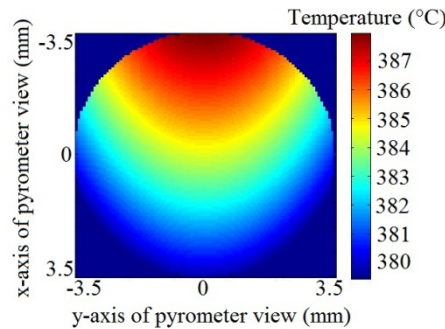


**Figure 3.2: Example of masked ‘pyrometer field of view’ generated using Matlab for model comparison with experimental results. The dark blue areas in the corners of the image represent ‘Not a Number’ values.**

The results show that the accuracy of the model falls to within different bounds for each material. The Silicon Carbide was matched to a fairly strong degree by the model, falling 4% and 3% outside the confidence bounds for 3m/min and 4m/min respectively. Considering that parameters such as temperature dependence of material properties were not taken into account at this point, the results were encouraging. ULE, on the other hand, was matched less strongly by preliminary results, with 3m/min and 4m/min predictions falling 24% and 6% outside of the confidence bounds respectively. Although the 6% value is not nearly as far off as the other, the issue arises from the lack of accounting for the absorption dependence on speed. This is something to be

addressed when implementing the transformation which was developed after these initial results were tested.

A positive upshot of the preliminary investigation is that the results show a correlation between the model and the experimental work in a broad sense, even if the correlation is not well defined. Through devising and performing further testing of experimental work, the capabilities of the model can be assessed more rigorously and the potential for identifying improvements exists.



## 4. MATERIALS AND METHODS

### 4.1 Materials

#### 4.1.1 Substrates

Two main materials were chosen for investigation: Corning Ultra Low Expansion Glass (ULE) and Silicon Carbide (SiC). Three variants of SiC were taken for investigation; two substrates of Trex chemical vapour composite SiC of differing surface quality and a porous Boostec SiC substrate with unknown but relatively poor surface quality. Substrate surface dimensions are:

- ULE – 100mm (W) x 100mm (H)
- SiC disc (Trex) – 100mm Ø with 80mm Ø polished area
- SiC square (Trex) – 100mm x 100mm
- SiC disc (Boostec) – 100mm Ø

Also used for thermal characterisation is a silicon wafer. This is used for RAP processing and measuring temperature of the plasma plume. The dimensions are 200mm Ø and 0.7mm thickness.

Additionally, for the spectrometric measurements of Trex SiC, an 80x80mm square of the same material was used. This was of same specified surface quality as the larger square, so is treated as equivalent for the purposes of modelling and experimental, even though the 100x100mm square was the one used for the laser heating.

#### 4.1.2 Sample preparation

Note: The preparation of the substrates outlined within this section occurs after the spectrometry measurements outline in section 4.2.1. Only two substrates were instrumented for contact surface temperature measurements, the Trex SiC disc and the ULE.

The contact method selected to measure laser induced temperature rise used RTD sensors. This is because they are a high accuracy contact method with a low thermal mass. Their availability in small physical sizes allows for precise positioning of the sensor relative to an incident laser beam to decrease locational errors in modelling. The RTDs used were Pt100 sensors of 2mm by 2mm surface area with a flat sensor area.

The configurations were selected to obtain maximum useful data possible across the width of the substrate. In the case of the ULE, 5 sensors were selected as the substrate had a homogenous surface quality over the width of the substrate. They were positioned

equidistantly at 20mm from one another as this was the maximum distance possible while fitting all 5 sensors onto the surface, and it is thought that with the laser passing no more than 5mm from the sensors, the inter-sensor distance would be sufficient for no interference between measurements. When considering a SiC disc, only 3 sensors were used as the substrate's useful high quality surface was only 70mm in diameter, but the same qualification with regards to inter-substrate distance applied.

The sensors were adhered to the substrates using a steel-based 2 part adhesive. The amount used to stick the sensors to the substrate was minimal, as little as it was physically possible to apply by human hand. This was in order to reduce the extra factors influencing the observed temperature by the RTDs. Images of the adhered sensors on the substrates can be seen in Figure 4.1. This particular epoxy was chosen as it tolerates high temperature for short periods of time (over 300°C for up to 10 minutes) which was suitable for the target temperatures on the substrates.

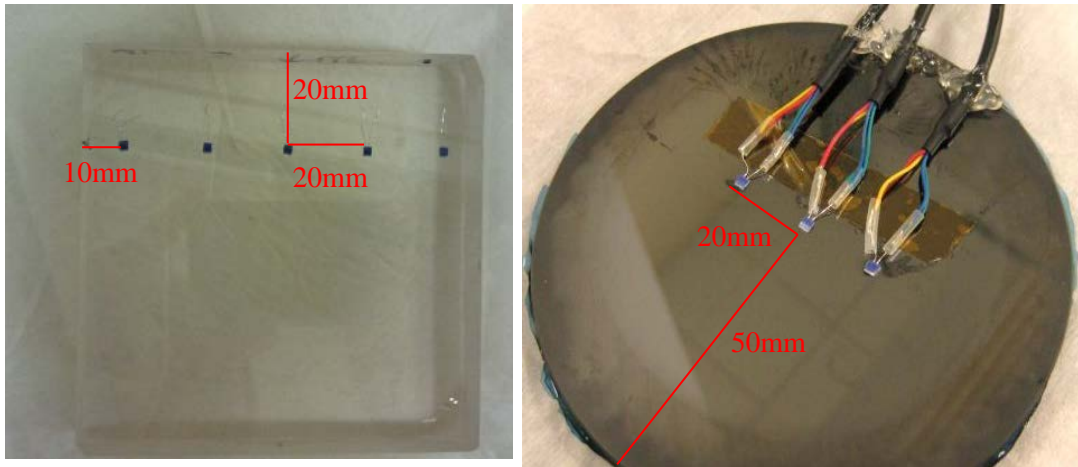


Figure 4.1: Images of instrumented substrates, ULE (left) and SiC (right). The RTDs were attached with minimal adhesive. The kapton tape seen is to protect the substrate surface from contact with the connected wires that can be seen. The wires were secured to the substrates or their holders so as not to lose connection with the sensors.

## 4.2 Methods

### 4.2.1 Spectrometry

A Jasco FT/IR 6200 Fourier Transform infrared spectrometer was used to measure optical performance of optical materials. This instrument has capability to measure transmittance and reflectance of substrates at infrared wavelengths, between 1 and 200 $\mu$ m. From measurements of both transmittance and reflectance, a value for absorbed radiation by that particular substrate can be inferred. Due to the adaptable nature of the equipment, different reflectance measurements can be exploited, such as specular at

specified angles and spherical diffuse reflections. The equipment has an achievable resolution of up to  $0.25\text{cm}^{-1}$ , which provides a detailed data set over the range of wavelengths of interest.

Three substrates were used for the spectrometry work – the SiC square of sub-nm surface roughness, the porous SiC disc and the ULE square. The two SiC choices were made to give an idea of what a highest possible quality surface would reflect and what a lowest used quality surface would.

The wavelengths being investigated were those between  $10.2\mu\text{m}$  and  $10.7\mu\text{m}$ , the values between which a  $\text{CO}_2$  laser can guarantee operation. A wavelength of particular interest is  $10.6\mu\text{m}$  as this is the primary operating mode of the  $\text{CO}_2$  laser. The actual wavelengths measured were between  $9.5\mu\text{m}$  and  $11.5\mu\text{m}$ ; this measurement window gave some context to the actual wavelengths of interest.

For these measurements,  $4\text{cm}^{-1}$  was the resolution selected. Although the equipment has higher capability than this (as previously stated), this resulted in over 1900 measurements over the wavelength range, and gave a more acceptable time of measurement. Any higher resolution would prove to be excessive in terms of data points and time used for the measurement. The measurement accuracy for the equipment is quoted as being  $0.01\text{cm}^{-1}$  and the signal to noise ratio as 45000:1.

The specular reflection of the materials at  $65^\circ$  incidence angle was determined using the spectrometer with a generic specular reflectance accessory. This device, produced by Pike Technologies, allows for specular reflectance of a substrate to be measured between  $30^\circ$  and  $80^\circ$  angle of incidence. It uses wave guides to direct light from the spectrometer's light source onto the substrate surface. The angle was selected at  $65^\circ$  as this is the angle at which the laser in the LAPP system will be incident.

A liquid nitrogen-cooled gold coated integrating sphere was used as an accessory for the spectrometer to measure the reflectance of the surfaces at all angles. This was used to determine if the surface quality of the substrates selected was sufficiently high such that scattering may be disregarded as an error factor in the specular reflections. If the spherical diffuse measurement using the integrating sphere was lower than the specular reflection measurement at wavelengths of interest, scattering will not influence the light's reflections at the specified angle. Spherical diffuse reflection is effectively a measurement of the surface's reflectivity over a range of angles, used for a control value in this case.

The environmental effects within the chamber need to be taken into account in this spectrometry system, as it is not a vacuum containment or sealed. To account for this the machine was programmed to take a series of repeat measurements over a time period of approximately 3 minutes, amounting to 128 repeat measurements taken during

this time. This high volume of repeats is a large enough sample of data to minimise all atmospheric and environmental issues to essentially nil.

#### 4.2.2 Surface temperature measurement

##### 4.2.2.1 Resistance temperature detectors

The two instrumented substrates mentioned in section 4.1.2 were taken for investigation of the temperature induced by transient CO<sub>2</sub> laser beam using contact methods. The intention of the work was to use an optical and laser setup similar to that which was implemented in the LAPP machine to scan a laser spot over a substrate using a motion stage to create relative motion.

The optical configuration required for the testing can be seen in Figure 4.2. The optics were implemented in such a way that the substrate distance could be varied to produce different spot sizes whilst still maintaining an beam spot as close to round as possible. For the purposes of modelling the beam spot is taken to be completely round – this cannot be guaranteed, only approximated from utilising a beam analyser. The beam analyser was utilised at a known distance from the laser shutter after the optical configuration. This allowed for calculation of the distance at which the substrate should be positioned in order to obtain a circular beam spot of the correct size.

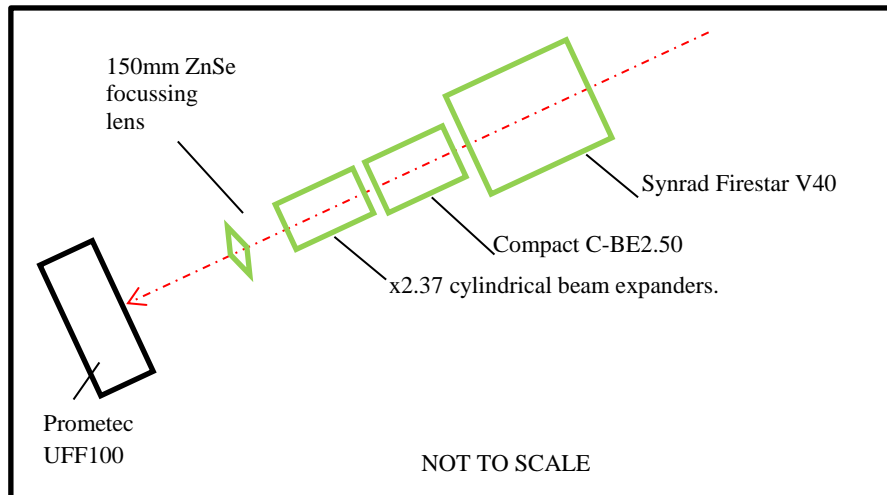


Figure 4.2: A schematic of the optics involved in undertaking the experimental work investigating laser induced temperature. The Synrad Firestar laser has its raw beam expanded both homogeneously and then in one axis separately to enlarge the beam and make it cylindrical. This is to account for the 65° incident angle of the beam onto the intended substrates and to allow for a smaller minimum spot size. Then the beam is focussed using a Zinc Selenide lens. In this diagram, the Prometec UFF100 beam analyser can be seen, which is used for experimentally determining the beam parameters; this does not remain during thermal investigation.

Aside from the positioning distance of the substrate, the optical configuration remains the same for these tests. The distance is varied depending on the material and the desired spot size. For ULE the desired spot size is 2mm radius and for SiC the desired spot size is 400 $\mu$ m, and distance from the focus was adjusted accordingly.

There are some other components that remain unchanged for the tests in order to maintain a consistent environment from which to obtain results. An Aerotech direct-drive linear stage with travel distance of 100mm travel was used for all experimental runs, which allowed for assessment of the transient nature of the laser beam spot relative to the substrate surface. This stage carried the substrate to generate a relative travel path of the laser spot.

The overall experimental setup can be seen in Figure 4.3.

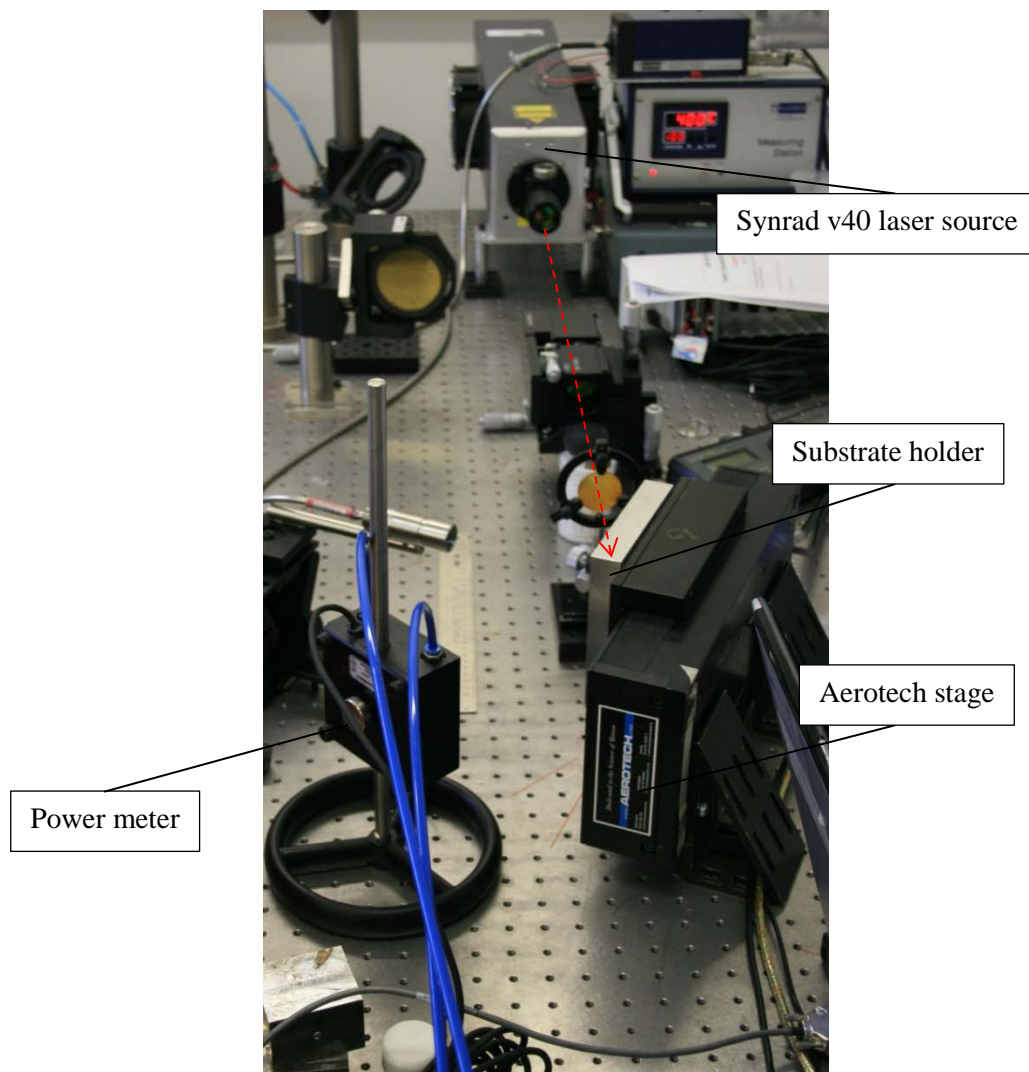
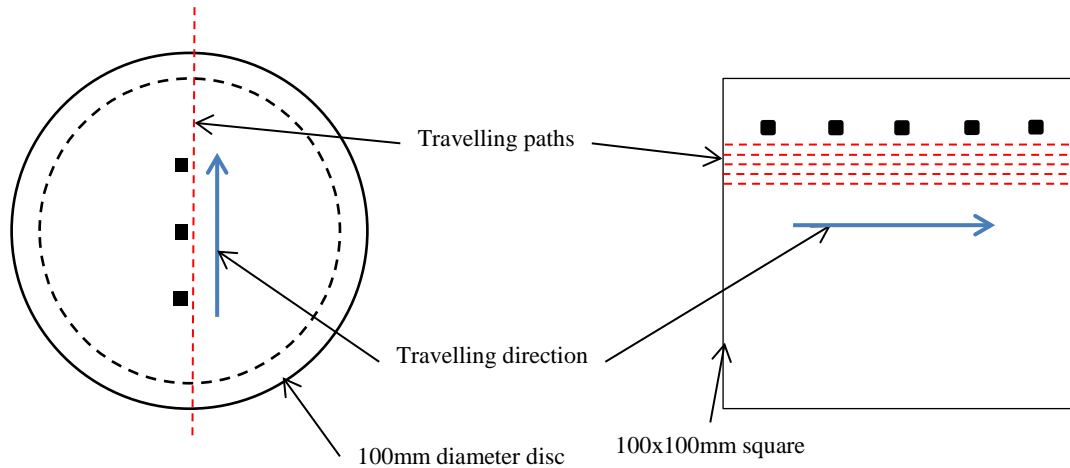
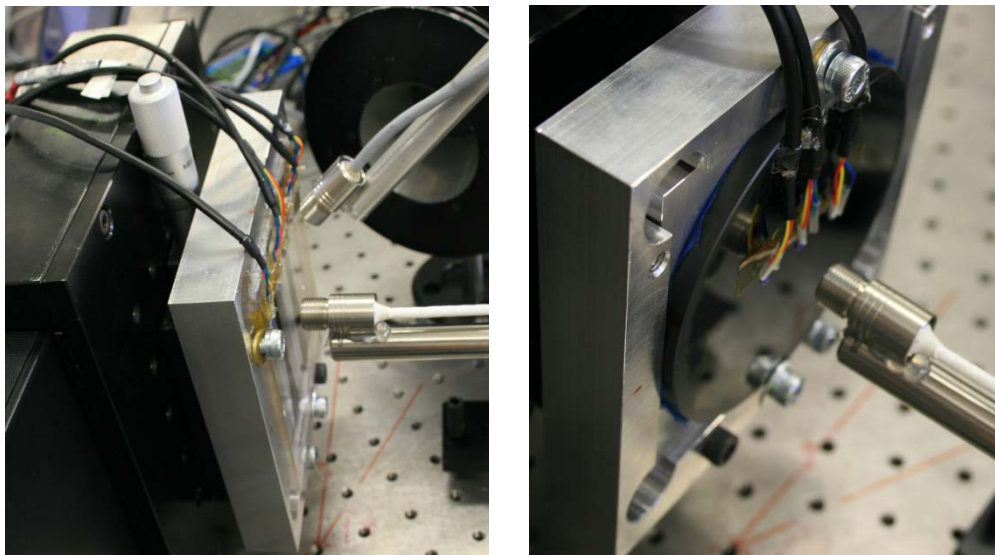


Figure 4.3: Setup for experimental measurement of transient laser beam induced temperature. Laser beam path can be seen indicated by a red dashed line. It is emitted from the laser source, passes through the optical configuration indicated in Figure 4.2 and strikes the substrate. A water cooled power meter is used to monitor reflections and terminate the beam.

The laser paths past the sensors are demonstrated in Figure 4.4. Only a single pass was performed on SiC as the surface roughness on that single path had been characterised using white light interferometry, so the decision was made to just select one travel path and vary the feed speed. Since the ULE had a homogeneous surface quality, more travel paths were investigated to obtain as much data as possible at several distances between laser travel and sensors. To see the substrates in position for processing, see Figure 4.5.



**Figure 4.4: Diagrams demonstrating the travel paths of a laser spot relative to the substrates whilst measuring transient laser-induced surface temperature using RTDs. SiC – laser spot centre passes along line 300 $\mu$ m from near sensor edge; ULE – laser spot centre passes along lines 2, 3, 4, 5mm from near sensor edge.**



**Figure 4.5: Images showing the physical setup of an instrumented ULE (left) and SiC (right) substrate in the holder in position for temperature measurements. The silver sensors that can be seen near the substrates are pyrometers used for non-contact temperature measurements.**

The process parameters to be varied in the case of ULE are laser power, process feed speed and sensor-laser distance. The parameters for this material can be seen in Table 4.1. After some preliminary testing on SiC it was determined that to obtain useful information from the sensors without damaging the substrate, the power had to be kept high (95% of laser capability) and therefore the only varied parameter measured by RTD was the feed speed variation. The parameters are shown in Table 4.2.

**Table 4.1: Experimental parameters investigated using RTDs for ULE; all paths use all distance and power combinations.**

Laser powers [W]	10	20		
Feed speeds [m/min]	3	4	5	
Laser path distances [mm]	2	3	4	5

**Table 4.2: Experimental parameters investigated using RTDs for SiC disc; all paths use all distance and power combinations.**

Laser powers [W]	35	47.5		
Feed speeds [m/min]	0.5	1.5	2	
Laser path distance [ $\mu\text{m}$ ]	300	400	500	

#### 4.2.2.2 Pyrometers

The non-contact method of temperature measurement utilised the same optical and stage configuration as the contact method to induce a temperature rise – it was the measurement system which was different.

Three substrates were investigated using pyrometers, the two Trex SiC substrates – one of which was instrumented with RTDs also and had the central polished area – and the instrumented ULE. Measurements were taken simultaneously using the RTDs and the pyrometer in the cases where the instrumented substrates are used, however for the purposes of this body of work the sets of data are considered separately.

Three different pyrometer setups were used to determine temperature rise. The first pyrometer was for direct temperature rise measurements perpendicularly over the area of laser incidence, see Figure 4.6. This was positioned as close as possible to the substrate without interfering with the laser propagation (10mm stand-off) so as to minimise the field of view. This was intended to give maximum possible observed temperature rise, as it was expected that with particularly small beam spots that the peak temperature would occur in a localised area. This pyrometer setup is easiest to model and will provide best possible results. In cases where another pyrometer configuration was used in conjunction with this one and the field of views would strike the other

pyrometer otherwise, the stand-off of this pyrometer was increased to 15mm, and this is noted accordingly with the results.

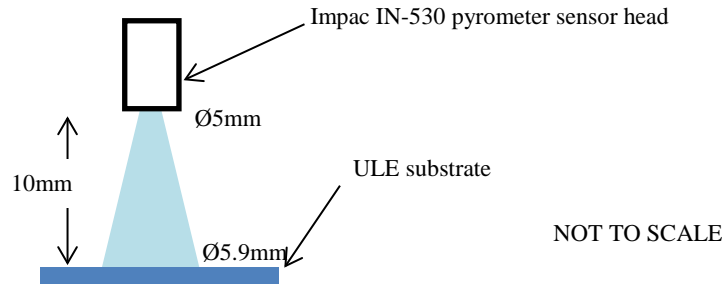


**Figure 4.6: Perpendicular pyrometer at 10mm stand-off, leading to a 5.9mm field of view at the substrate surface. This pyrometer will be positioned directly above the laser incidence zone.**

The other two pyrometers were inclined at 45° angle to the substrate surface, see Figure 4.7. The reason for this is that in the LAPP system, the pyrometer for monitoring substrate temperature is limited in its physical location by the constraints of the machine, and cannot be perpendicular to the surface as this would either be the location of the RAP torch or in line with the laser's reflections, causing it damage. Therefore, the 45° angle was introduced. One of the two angled pyrometer configurations was positioned over the laser incidence zone, see Figure 4.8; the other is 50.4mm away from this zone in a direction behind relative laser motion, see Figure 4.9. This means essentially the pyrometer is travelling relative to the surface in line with but 50.4mm it was behind the laser and saw residual temperature. The latter of these two cases is the one which will be present in the LAPP machine, but the other configuration is included so as to investigate the effect that the inclined field of view has on measured temperature when compared with the perpendicular pyrometer.

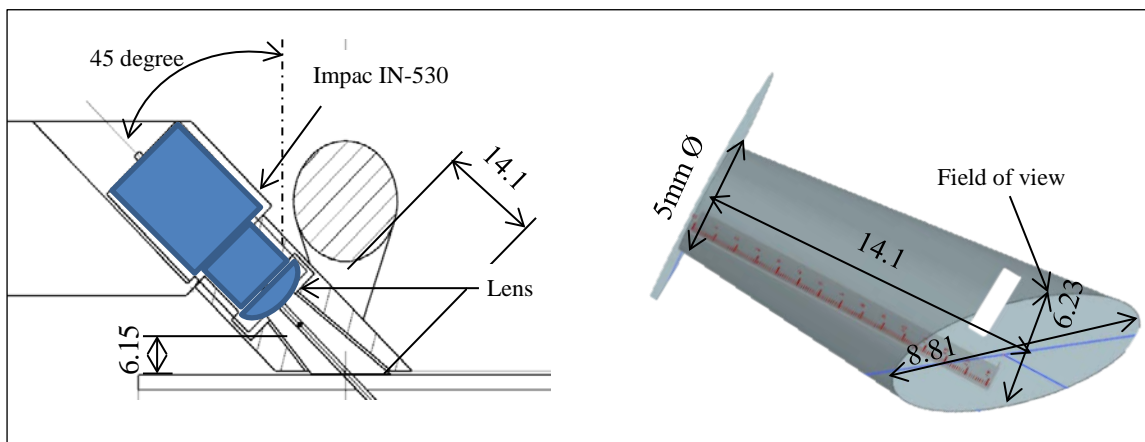


**Figure 4.7: Configuration and field of view of a 45° angled pyrometer. The setup is limited by a protective shielding placed around the pyrometer head in the LAPP machine to protect the pyrometer lens from the plasma environment. The resultant field of view, as seen to the right hand side of the diagram is elliptical.**



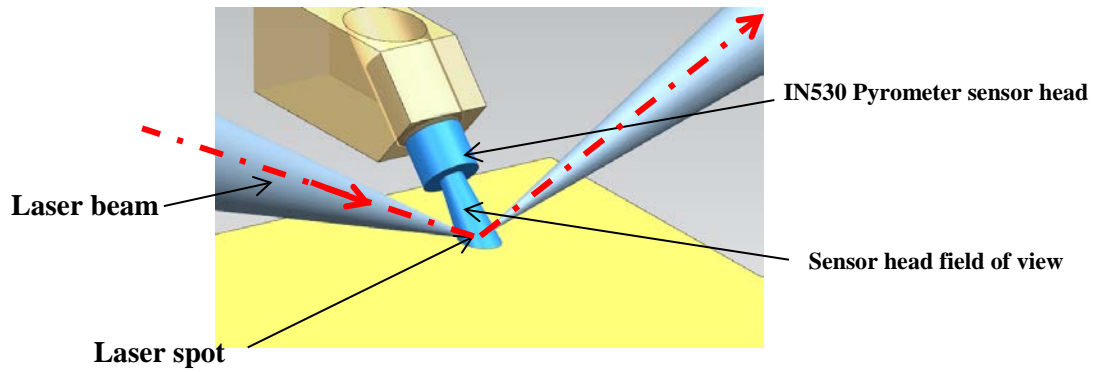


Figure 4.8: Laser incidence zone 45° angled pyrometer configuration. With dimensions demonstrated in Figure 4.7 this pyrometer measures temperature where the laser strikes the substrate.

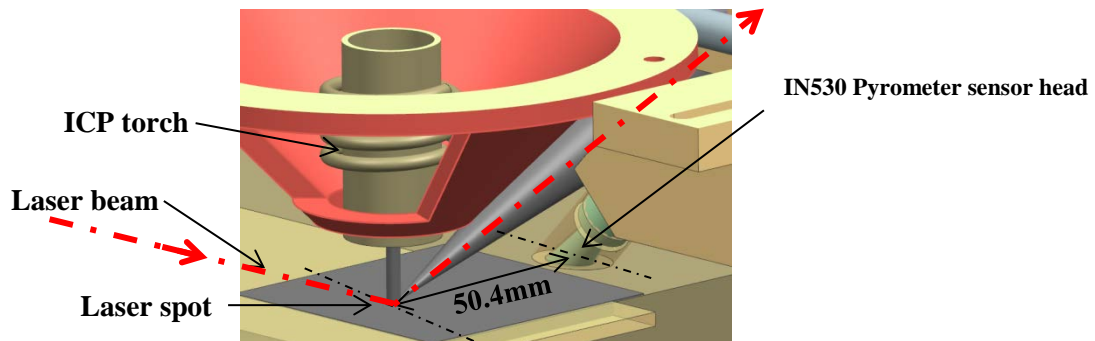
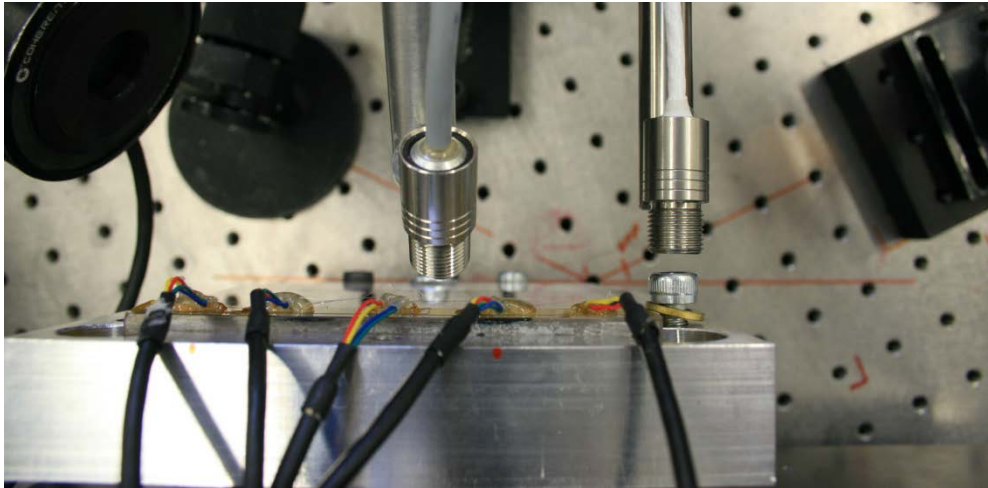


Figure 4.9: 50.4mm displaced zone 45° angled pyrometer configuration. With dimensions demonstrated in Figure 4.7 this pyrometer measures residual temperature on the substrate surface after 50.4mm further has been travelled on the same motion axis.

Different configurations of pyrometers are used to ensure as much data as possible is obtained. Although each pyrometer head has its data modelled and analysed separately, much of the data capture was implemented contemporaneously. In Figures 4.10 and 4.11, images of the each different pyrometer setup can be seen, demonstrating typical configurations which were implemented to capture data.



**Figure 4.10:** Top-down image of an example of pyrometer data capture, in this case on ULE. The pyrometers that can be seen are over the laser incidence zone at 10mm standoff (right) and at 45° incidence angle displaced by 50.4mm in the axis of substrate travel.



**Figure 4.11:** Side-on image of an example pyrometer configuration, in this case on a SiC square substrate. The pyrometers observed are both imaging the laser incidence zone, with one 45° angled pyrometer and the other at 15mm standoff perpendicular to the substrate surface.

The process parameter combinations investigated are laid out for ULE in Table 4.3, for the instrumented SiC disc in Table 4.4 and for the SiC square in Table 4.5. The pyrometer configurations used for both ULE and the SiC disc were: normal over the laser incidence zone at 10mm stand-off and at 45° displaced by 50.4mm. The pyrometer configurations used for the SiC disc were: normal over the laser incidence zone at 10mm and 15mm stand-off, at 45° displaced by 50.4mm, and at 45° over the laser incidence zone.

**Table 4.3: Experimental parameters investigated using pyrometers for ULE; all distance and power combinations are investigated.**

Laser powers [W]	10	20	
Feed speeds [m/min]	3	4	5

**Table 4.4: Experimental parameters investigated using pyrometers for SiC disc; all distance and power combinations are investigated.**

Laser powers [W]	35	47.5	
Feed speeds [m/min]	0.5	1.5	2

**Table 4.5: Experimental parameters investigated using pyrometers on SiC square; all distance and power combinations are investigated.**

Laser powers [W]	35	47.5	
Feed speeds [m/min]	0.5	1.5	2

#### 4.2.2.3 Thermocouples

Thermocouples were used to measure the temperature profile of a RAP torch using a silicon wafer. The silicon wafer was used as it is thin and conductive. This means that the harsh environment can be minimised as a factor affecting results. By using the wafer with sensors adhered to the rear side, the highest possible temperature can be measured (as close as possible to the top surface temperature) without risk of damaging the sensors. If a pyrometer sensor head or contact sensor was placed above the substrate or on top of it then the plasma could etch these items and destroy them or affect results.

The thermocouples were adhered in a similar fashion to that of the RTDs, to the back of the wafer using the same adhesive. The instrumented substrate can be seen in Figure 4.12.

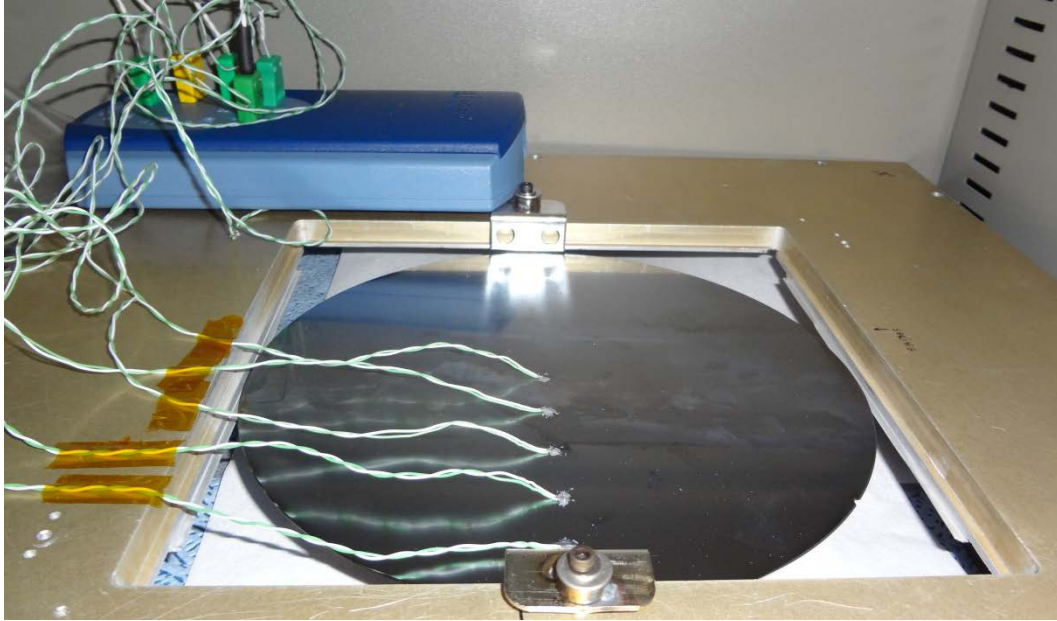


Figure 4.12: Back of the instrumented Si wafer substrate for measuring RAP torch temperature profile. Thermocouples, adhered to the substrate, are connected to a TC-08 data logger. The substrate is in a holder used to affix the surface at the correct height within the Helios 1200 machine.

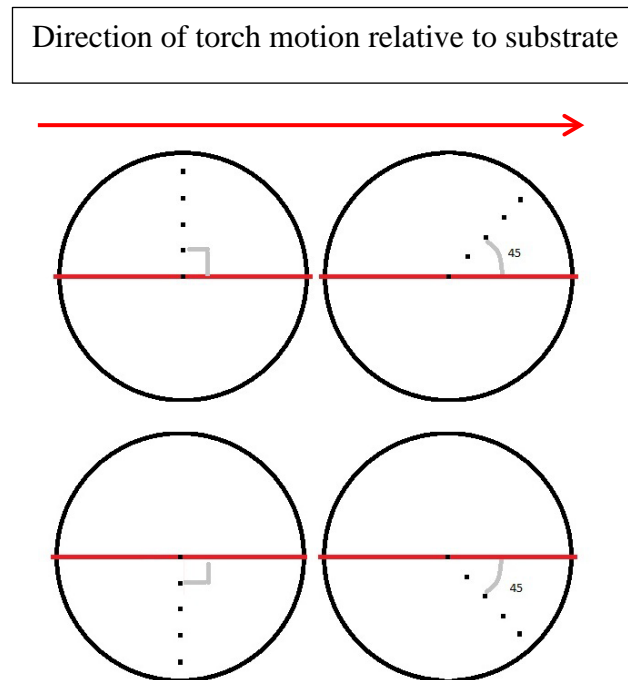


Figure 4.13: Geometries of thermocouple configurations when observed relative to a substrate and the motion of the RAP torch relative to that substrate. The thermocouples are represented by the black squares in this case. Substrate diameter is 200mm.

Four orientations of the sensors relative to the path of the torch are considered and conducted. This is to assess the symmetry of the thermal footprint of a RAP torch and to obtain data sets for maximum possible information to compare with modelling. The geometries of the configurations can be seen in Figure 4.13. Typical RAP process conditions were investigated, which can be seen in Table 4.6, with the variable parameter being process speed.

**Table 4.6:** Experimental parameters investigated using thermocouples on a Si wafer for each of the thermocouples geometric configurations. Torch power and stand-off are typical for RAP processing and feed speed is the variable.

Torch RF power [W]	1200			
Feed speeds [m/min]	1	2	3	4
Torch stand-off [mm]	6			

## 5. RESULTS AND DISCUSSION

In this section, the results from each set of investigations is presented and discussed. The results will be presented with reference to modelling simulations where appropriate and as a form of analysis or an informant to the modelling work.

### 5.1 Spectrometry

The transmitted portion of the light was the first parameter measured. This is dependent largely on the individual substrate selected, due to absorption of a material being dependent on thickness of that material – otherwise referred to as depth when considering the propagation of the light perpendicular to the substrate surface. The ULE sample was a polished 100mm square surface with a thickness of 20mm. The first Trex SiC substrate was a 100mmØ disc of 8mm thickness which has been polished within Cranfield University Precision Engineering Institute to within 20mm of the substrate edge. The second Trex SiC was a high quality 80mm by 80mm surface of 0.1nm RMS surface figure and thickness of 8mm. The sintered SiC was a 100mmØ disc of 8mm thickness; the surface was not polished in this instance, and thus the exact quality was not known. Therefore, the data about this substrate is extra information for the sake of interest.

Transmission through a bulk semiconductor, like the silicon carbide in question here, was expected to be negligible at infrared wavelengths. This was confirmed by experimental results, with  $<<0.1\%$  transmission of light through the Trex SiC across a wavelength range of 1.5-16.7 $\mu\text{m}$ . The values obtained were consistently of the order of the noise of the system, and from this we can ascertain that transmission of bulk SiC substrates is effectively nil. The ULE substrate had  $<1\%$  transmission consistently for all measured values between 5 $\mu\text{m}$  and 16.7 $\mu\text{m}$ . Below 5 $\mu\text{m}$  there was significant transmission, but this information is surplus to current requirement as the laser that will be used in laser assisted plasma processing does not operate in these wavelengths. The values of below 1% for the remainder of the data set are treated as negligible in this investigation.

The results for the two main optical materials for reflectivity, ULE and Trex SiC, are given in Figure 5.1 and Figure 5.2 respectively.

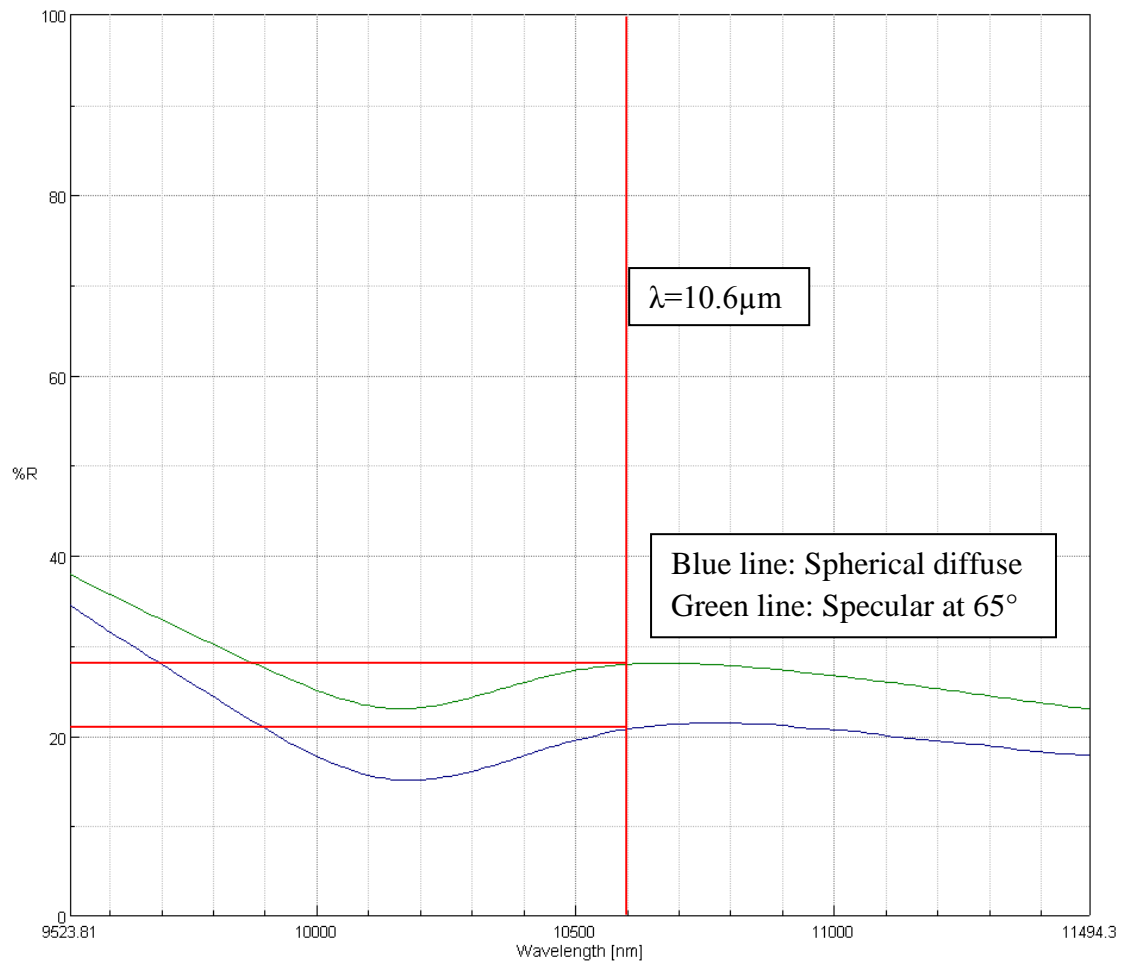


**Figure 5.1: Plot of percentage reflectance with wavelength of 65° incident angle light and spherical diffuse light in the 9.5-11.5μm wavelength range for polished ULE glass.**

As can be seen in Figure 5.1, for ULE glass the specular reflectance at 65° at 10.6μm is 28.5%. This value is higher than the 21.5% reflectivity measured using an integrating sphere, meaning there are no important scattering effects that will affect laser interaction with polished ULE surfaces when using these light parameters. The low reflectivity that characterises ULE means that it will absorb a sufficiently large amount of radiation to induce a substantial temperature rise even at relatively low laser powers.

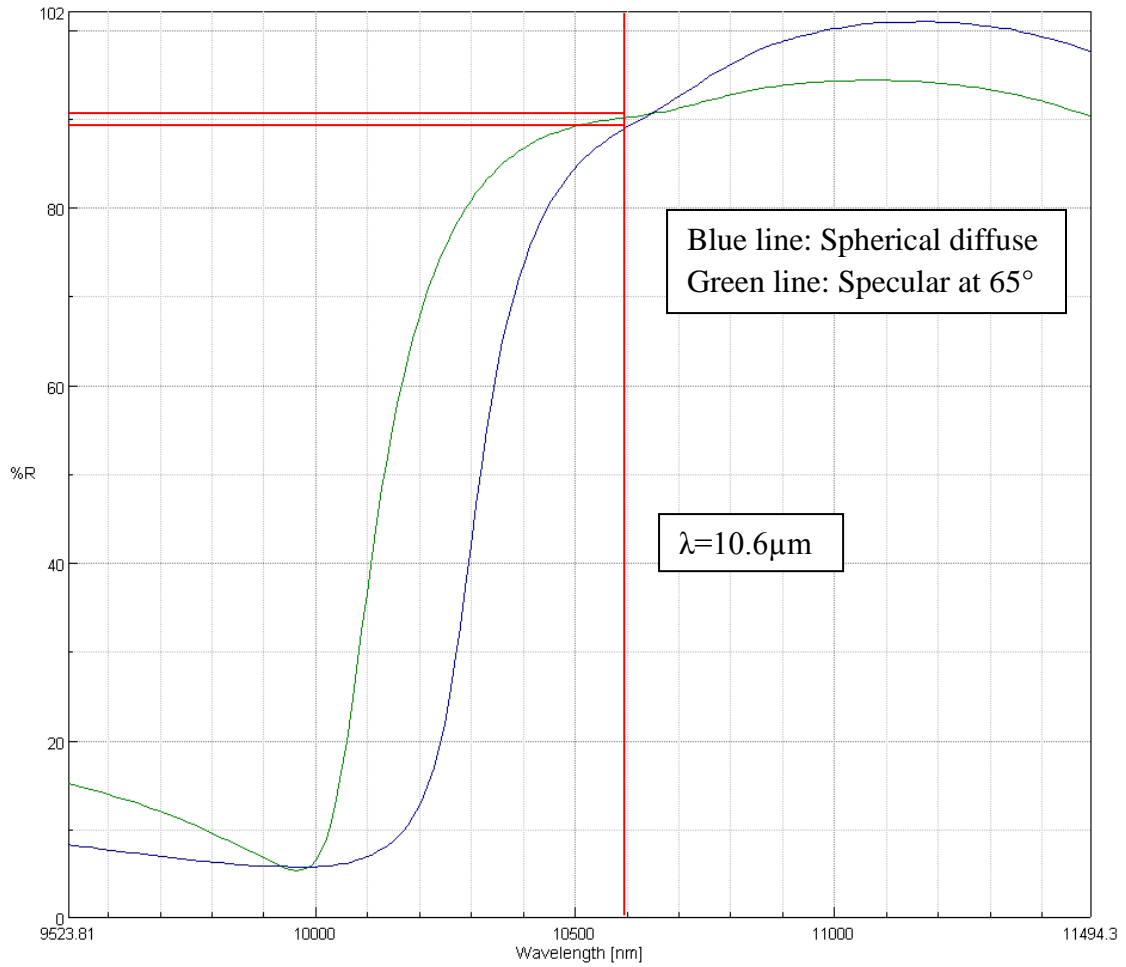


**Figure 5.2: Plot of percentage reflectance with wavelength of 65° incident angle light and spherical diffuse light in the 9.5-11.5μm wavelength range for a Trex SiC disc.**

Conversely to the ULE substrate, at 10.6μm wavelength Trex SiC is highly reflective. On the first SiC substrate, the disc polished by Cranfield, the specular reflection at 65° is 90.5%, higher than the spherical diffuse reflectance which is 89.5%. This means that scattering effects are not an issue for laser light on Trex silicon carbide under these parameters. The high reflectance that characterises SiC means that the substrates will require significant laser power to induce a substantial temperature rise when compared with those powers required by ULE for the same laser spot size. Another factor that must be dealt with accordingly when considering the high reflectance of silicon carbide is the reflected laser light itself. This light will be diverging (as it would have been focussed at the surface) and of very high power density, and must be terminated appropriately as this is an extremely dangerous by-product if not handled correctly.



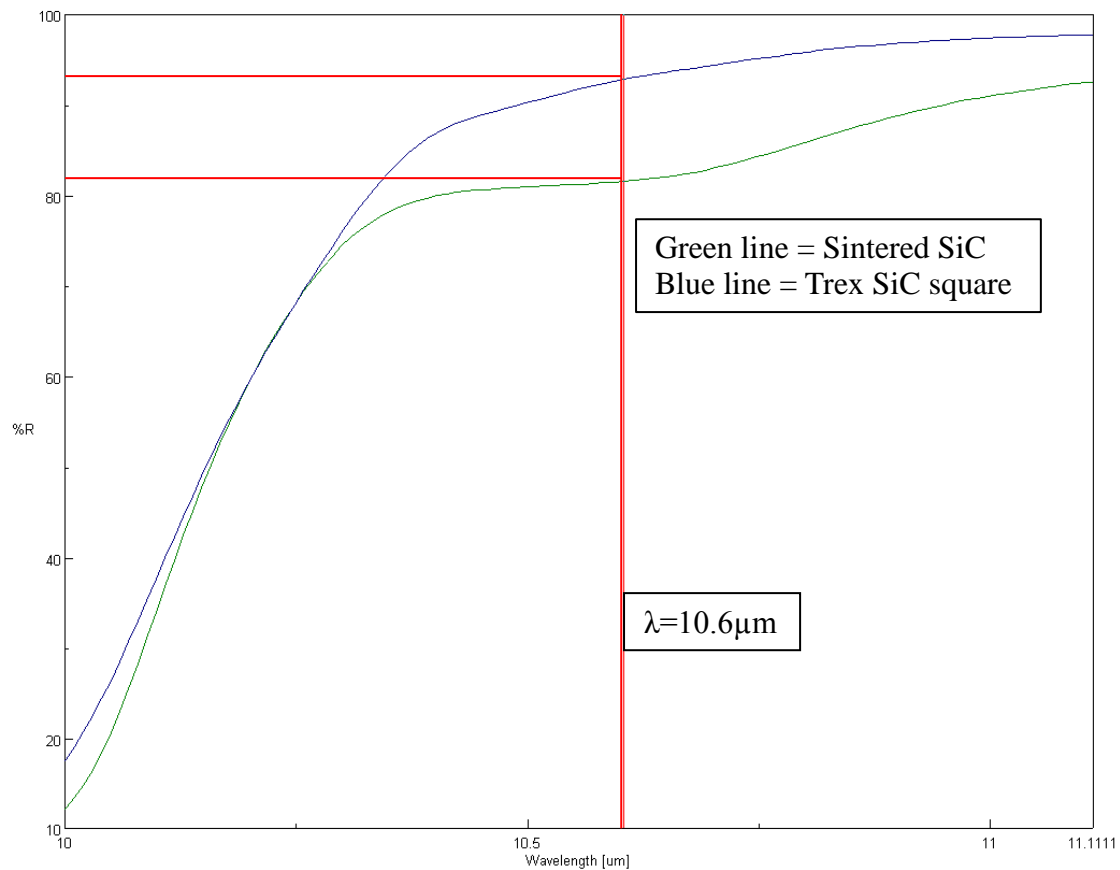


**Figure 5.3: Plot of percentage reflectance with wavelength of 65° incident angle light in the 9.5-11.5μm wavelength range for a Trex SiC square of highest achievable surface quality and also for sintered SiC of relatively poor surface quality.**

Figure 5.3 demonstrates the reflectance of silicon carbide with poor surface quality and excellent surface quality (RMS 0.1nm). The Trex SiC and sintered SiC have 93.0% and 82.0% reflectivity respectively at 10.6μm. The 93.0% reflectivity for the high surface quality SiC is representative of the highest achievable reflectivity on this substrate as it is the best achievable surface quality. This is because it has been supplied with this quality from the manufacturer, and has roughness and surface form better than is achievable using RAP. Therefore, any substrate being used will be of this quality or lower during LAPP. The poorer quality surface will absorb more laser light, so this must be accounted for if a poor quality surface is being processed using LAPP.

A limitation of the work performed using a spectrometer is that it was conducted at room temperature. The intention of the laser in LAPP is to increase the surface temperature so as to increase etching. As well as the laser as a heat source there is also the plasma heat source to consider. The reflected portion of the light measured in this work is valid at the beginning of processing, but as the substrate heats up the reflectance will change. Over the course of processing, a different percentage of the light will be

reflected which will vary with time. This is clearly a parameter that needs to be explored.

## 5.2 RTD results

Figure 5.4 shows an example of the time development of the temperature observed by five RTDs on a ULE substrate as a laser spot passes by. A clear pattern can be observed through Channels 1-4 as with passing time the laser induces a temperature rise measured by the sensors most strongly after the spot has passed by. The spot, of 2mm diameter, passes by the sensors with its centre 2mm from the near sensor edge in this case. If first moves past the sensor marked Channel 5, progressing past the sensors to sensor 1 last of all. This is reflected in the fact that the temperature rise can be observed occurring first on Channel 5.

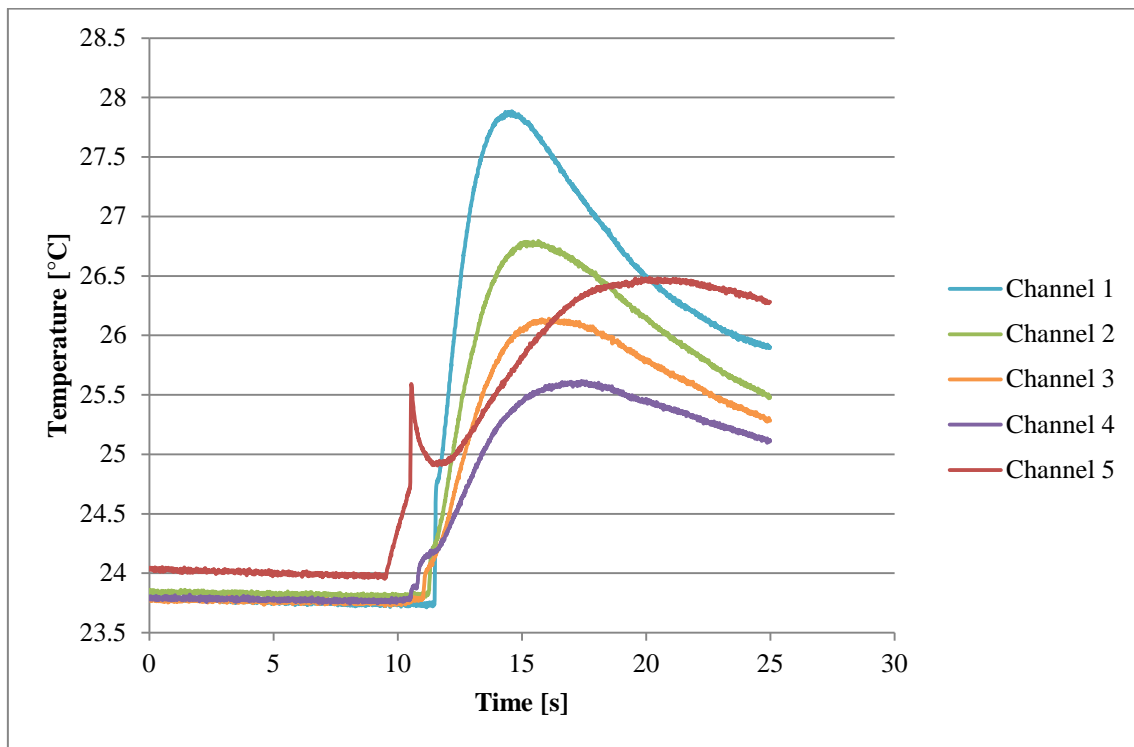


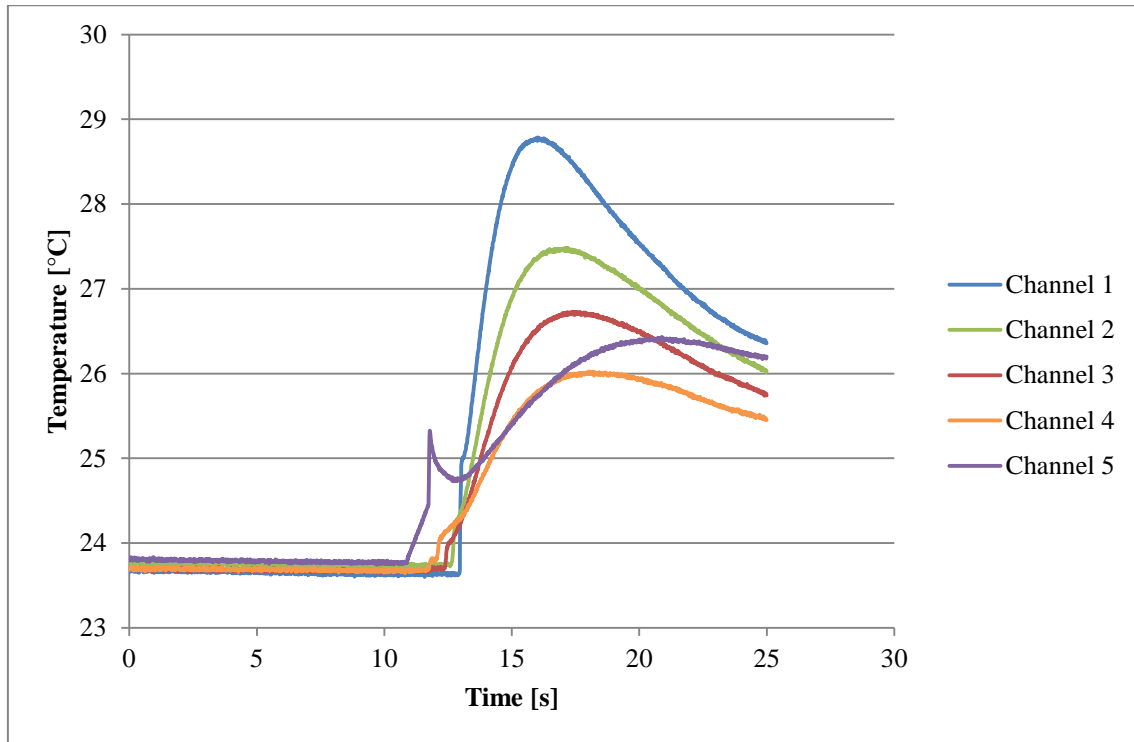
Figure 5.4: A plot of the temperature rise on ULE from processing using a CO<sub>2</sub> laser at 5m/min feed speed with a 2mm beam spot and 10W power, as measured using RTDs, with the near sensor edge 2mm from the laser beam spot centre.

Channel 1 has the highest temperature rise due to the cumulative effect of the heat within the substrate permeating through. This means that it measures the highest peak temperature. Temporally, Channel 1 reaches its temperature peak first as it is near the

edge of the substrate so less backwards propagating heat reaches the RTD after the spot has passed, whereas the other sensors have some of the additive heat contributing to their peaks even after the spot has passed, meaning it takes longer to reach their maximum.

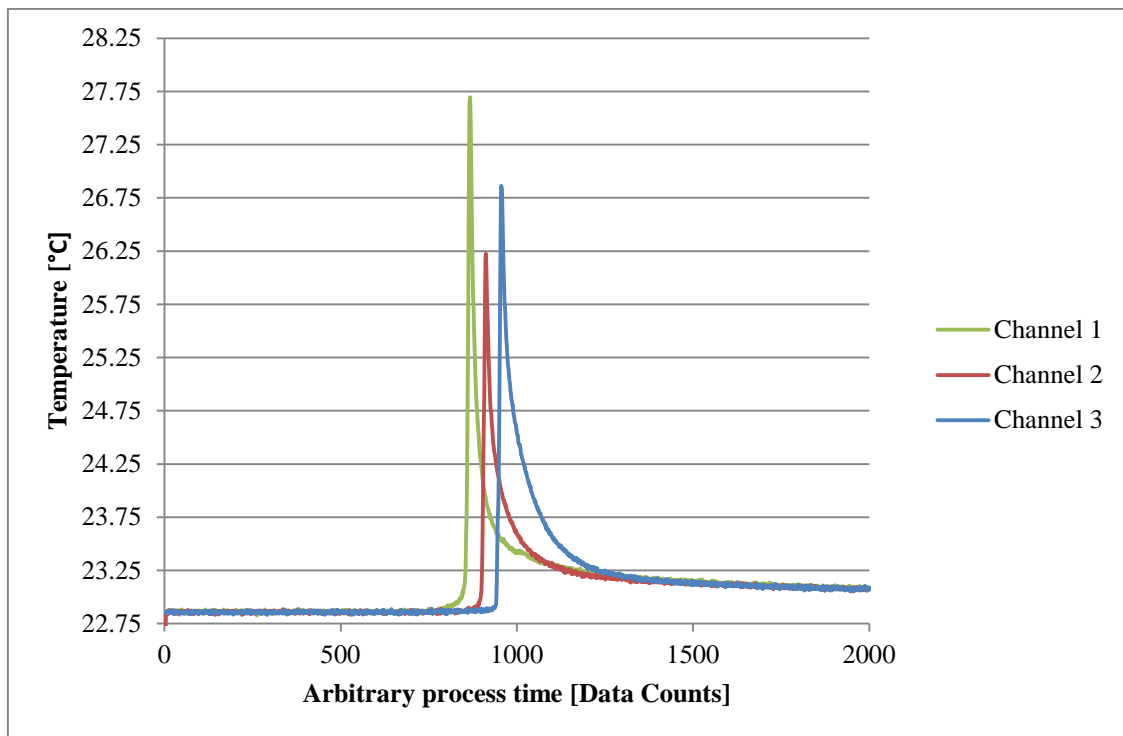
Channel 5 has an anomalous shape to its temperature measurement with time. This is an anomaly due to the laser striking a copper strip as a run-on to the substrate, which allows stray reflections off the edge when transitioning between the copper and the substrate. The stray reflections affect the sensors nearest to it, especially Channel 5. There is also a very small but noticeable effect in sensors 4 and 3. The Channel 5 sensor may be affected by the laser light striking it directly, thus displaying a different profile of temperature with time. This can be observed in Figure 5.4 by Channel 5 reaching its peak last and having a higher than expected peak temperature.

Figure 5.5 shows another example, with the feed speed set at 4m/min and otherwise identical process parameters to Figure 5.4. Similar features can be observed to the previous Figure, with the addendum of stating that the temperature peak is approximately 1K higher for each sensor than at the faster speed.



**Figure 5.5:** A plot of the temperature rise on ULE from processing using a CO<sub>2</sub> laser at 4m/min feed speed with a 2mm beam spot and 10W power, as measured using RTDs, with the near sensor edge 2mm from the laser beam spot centre.

Figure 5.6 shows three RTDs on a Trex SiC disc measuring temperature in a similar fashion to the aforementioned measurements on ULE, but with different process parameters (see caption). The results show, that the middle sensor has consistently lower temperature readings than the other two channels, which is supported by other combinations of process parameters. Due to the minor difference in the detected temperatures (in this case 1.5K), the discrepancy could be explained in several ways. The most likely are either an inherent error in the RTD or error in the calibration of the sensor, or a slight variation in surface quality near that sensor. Since the absorption of CO<sub>2</sub> laser light by SiC is so dependent on surface roughness, even a small variation in roughness could potentially cause this kind of discrepancy on a sensor.



**Figure 5.6:** A plot of the temperature rise on SiC from processing using a CO<sub>2</sub> laser at 2m/min feed speed with a 400 $\mu$ m beam spot and 47.5W power, as measured using RTDs, with the near sensor edge 0.5mm from the laser beam spot centre. For the horizontal axis, each data count took approximately 10ms $\pm$ 3ms.

What is a key to analysis of the thermal properties of the LAPP system is a knowledge of how the components vary with changing process feed speed and laser power. In Table 5.1, a set of laser power and feed speed combinations is given for each RTD sensor at a time 4s after the start of the process on ULE. This time interval ensures that the laser has heated the substrate to the maximum possible level without any of the sensors having peaked at any feed speed. This selected time, although after the laser has finished processing the substrate, is still valid when compared to a modelled

temperature. Table 5.1 contains both modelling predicted and experimentally obtained data for the ULE substrate. The two materials are considered separately due to different required process parameters. The selection of measurements shown is for the laser spot centre passing 2mm from the near edge of the sensor.

**Table 5.1: Table of experimental [E] and predicted [P] temperature with variables of power and feed speed as measured by each RTD at a known time of 4s on ULE. RTD 5 is the first to be passed, RTD 1 is the last.**

Power [W]	Feed speed [m/min]	Temperature at t=4 s [°C]									
		RTD 1		RTD 2		RTD 3		RTD 4		RTD 5	
		E	P	E	P	E	P	E	P	E	P
10	3	27.0	28.9	25.9	28.1	25.4	27.3	24.8	26.3	24.8	25.1
	4	26.7	25.2	25.8	24.6	25.3	23.9	24.9	23.2	25.1	22.5
	5	26.0	23.2	25.4	22.8	25.0	22.3	24.7	21.8	24.9	21.3
20	3	30.2	37.8	28.1	36.3	27.0	34.5	26.1	32.5	26.1	30.2
	4	28.7	30.4	27.3	29.2	26.4	27.9	25.6	26.5	25.7	25.0
	5	27.8	26.4	26.6	25.5	25.8	24.6	25.3	23.6	25.6	22.6

It can be seen that the dependence of temperature on feed speed is a negative relationship – increasing feed speed decreases temperature. For the experimental work, this holds true for RTDs 1,2,3 for both power levels selected. However, for RTDs 4 and 5, at further distances from the laser spot at this time, the temperatures converge and in the case of 10W power overlap, because of the uncertainty in the experiments (see error analysis on pp51-52). For the predicted values, a slightly different relationship can be seen. While still a negative relationship, the temperature depends more strongly on the feed speed. This can be seen most clearly when looking at RTD1, where the difference between 3 and 4m/min is predicted to be 7.4K for 20W power, whereas the experimental values show only a 1.5K difference.

The dependence of temperature on feed speed is found to fit a second order polynomial equation for both prediction and experimental values, as data has been fit using Matlab curve fitting techniques. However, it is seen that the scaling factors are different for each set. The equation for a sample experimentally obtained set of data (10W, RTD2) is given by:

$$\text{Temperature} = -0.15 * (\text{feed speed})^2 + 0.95 * (\text{feed speed}) + 24.4$$

With the negative factor on the squared component. The predicted values for the same set of process parameters, however, give an equation as follows:

$$\text{Temperature} = 0.85 * (\text{feed speed})^2 - 9.65 * (\text{feed speed}) + 50.2$$

When considering the dependence of the temperature on the laser power, a relation can be seen which indicates temperature increasing with increasing power. For the experimental results, this is characterised by an approximately 25-30% increase in temperature rise from room temperature with doubling of laser power, compared with the scaling of the modelling values by doubling temperature rise from room temperature with doubling laser power. More levels of laser power need to be investigated to assess the dependence of the temperature on laser power experimentally.

The dependence of the temperature on feed speed should be governed by an inverse relationship according to the theory, with temperature rise being proportional to the reciprocal of feed speed. However, as stated above there is a closer fit to a polynomial relationship for the data when plotted. With further experimental work, and in conjunction with extra trials varying laser power, a more rigorous assessment of the temperature in relation to a combined power and velocity function could be performed and utilised as part of the characterisation of the laser/plasma hybrid system.

Table 5.2 contains experimental and predicted values for SiC using a similar format to above but with different process conditions. Since only a single power was investigated using SiC, feed speed is the key variable here. The RTD near edges are at a distance of 500µm from the centre of the laser beam spot. The RTD temperature peaks are so short in time due to the conductive nature of the material that each sensor must be assessed on for own time for its own speed, and this is accounted for in the modelling predictions.

**Table 5.2: Table of experimental [E] and predicted [P] temperature with variables of power and feed speed as measured by each RTD at a known time on SiC.**

Power [W]	Feed speed [m/min]	Temperature at peak [°C]					
		RTD 1		RTD 2		RTD 3	
		E	P	E	P	E	P
47.5	0.5	31.3	45.3	30.0	45.3	34.3	45.3
	1.5	29.0	29.6	27.1	29.6	28.3	29.6
	2	27.7	26.5	26.1	26.5	26.9	26.5

The temperature induced on silicon carbide is predicted to follow a negative relationship with feed speed; higher feed speed means lower induced temperature. The experimental results seem to imply a linear relation between temperature and feed speed, with the fitting equation for RTD 2 for example being:

$$\text{Temperature} = -2.6 * (\text{feed speed}) + 31.3$$

However, the fit for the predicted relation is a power law nonlinear relationship. The equation that describes it is:

$$\text{Temperature} = 34.6 * (\text{feed speed})^{-0.387}$$

This discrepancy between the modelling and experimental relations could be due to the lack of cooling effect of the substrate's surface into the surroundings in the model. This would act to linearize the relationship more, cooling higher temperatures more and lower temperature less.

The sources of error for the RTD work are actual equipment errors and positioning errors. The positioning errors are those introduced by the x-placement of the sensors relative to one another ( $\pm 0.50\text{mm}$ ), and the laser spot relative to the sensor edge ( $\pm 0.083\text{mm}$  after considering lenses). The actual errors in the equipment are  $\pm 0.3\text{K}$  inherent for RTDs, and power stability of the laser quoted as 5%. The two major contributors of the error are the laser spot positioning (resulting in a 7.8% temperature uncertainty) and the 5% laser power (resulting in 5% uncertainty in temperature). The other factors are negligible when compared with those for their respective measurements. These combine mathematically to give a  $\pm 9.3\%$  error in RTD measurements. The 9.3% error on values equates to a 2.5K real error value on a sample measurement value of  $27^\circ\text{C}$ . When compared with a typical temperature change of around 5K this is a significant portion (in this case 50%) of the temperature change.

For ULE, overall the model agreement is strong when modelling RTDs. The largest discrepancy above an experimental value is 8.2K and the lowest discrepancy below an experimental value is 3.6K. 19 of the 30 measurements sampled above fell within the experimental error. The general trends of temperature increasing with increasing power and temperature decreasing with increasing speed are upheld by the model and the experimental results. The sensitivity of the predictions to both of these factors is greater for the prediction however, with the temperature changing more rapidly with each parameter than the experimental results. It is expected that this is because cooling effects from the substrate surface are not taken into account, which act counteractively to change of parameters. This means that higher temperature is cooled more and lower temperature is cooled less. This factor is not accounted for in the model and would explain the difference dependence of temperature on the parameters.

Overall, the model works with some success in modelling RTDs on silicon carbide. The order of magnitude is correct, and at higher feed speeds (1.5 and 2m/min) achieves agreement with the experimental results to within the experimental error. With the implementation of a cooling rate influence, the slower feed speeds would hopefully be improved in matching the experiments.

### 5.3 Pyrometer results

#### 5.3.1 ULE

Temperature measurements on ULE using pyrometers are first analysed with respect to feed speed. Figure 5.7 shows the temperatures achieved under various process parameters as measured by a perpendicular pyrometer with 5.9mmØ field of view. It is seen that the feed speed is not the key parameter for investigation on this scale. Although there is some variation of measured temperature with feed speed, there is no decisive relation from the results obtained, at least on a scale where measurements using a pyrometer are concerned. A much more important factor is the laser power employed.

The laser power has a much more pronounced effect on the achieved temperature rise. At 4mm distance from the RTDs, the doubling of laser power at least doubles the achieved temperature rise for each investigated speed. At 3mm distance from the RTDs this conversion is not quite maintained, with a doubling of laser power resulting in 1.8 times the temperature rise. This is a much more powerful parameter to work with for increasing temperature than feed speed.

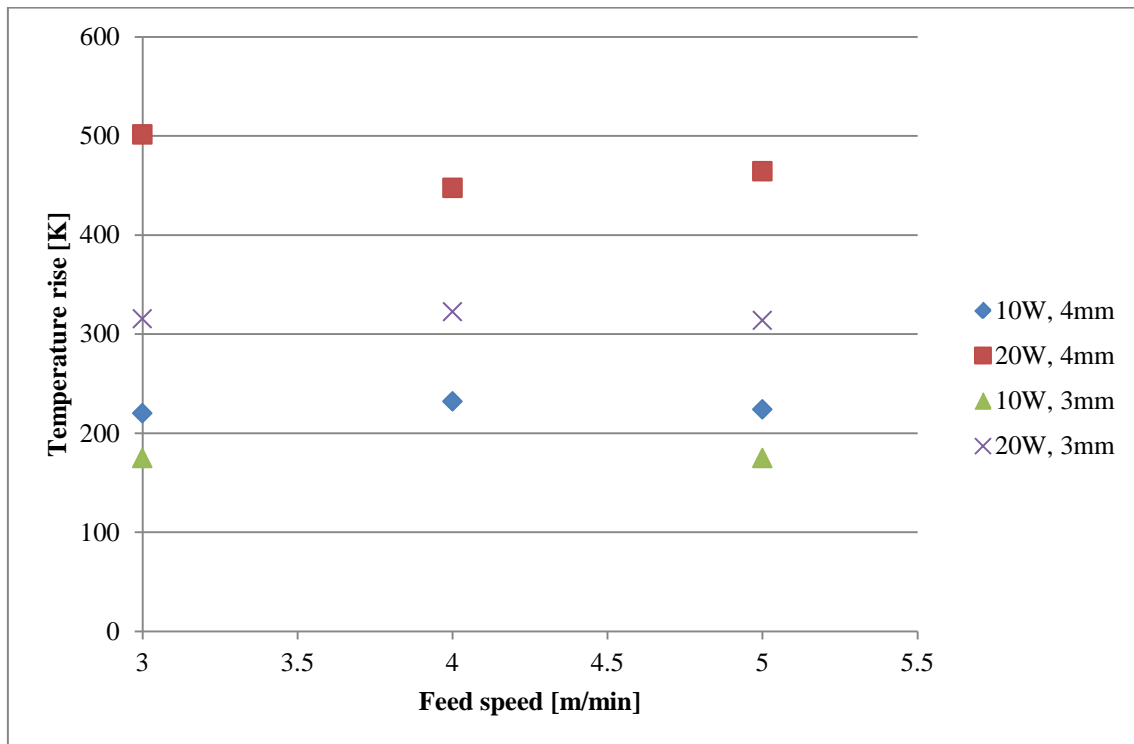


Figure 5.7: Plot of initial temperature rise above room temperature induced by laser on ULE with feed speed as measured by pyrometer.



Worth noticing is that the temperature values for 3mm from the sensors are lower than those at 4mm from the sensors, even though other process parameters are consistent. There are two possible explanations for this: misalignment of pyrometers or thermal influence of sensors. Since the pyrometer has positioning accuracy of no better than 500 $\mu$ m, it is possible that the pyrometer's field of view encompasses part of the RTD itself, and is therefore not measuring the substrates surface entirely, and this would clearly reduce the observed temperature. The other possibility, that the sensor's thermal mass is 'drawing' heat from the surface and reducing the actual surface temperature is also a possibility and could be occurring in conjunction with the first possibility. Both of these factors would reduce observed surface temperature using a pyrometer.

As Figure 5.7 demonstrates the initial raised temperatures measured by the pyrometer, it should be stated that the heating of ULE consists of two major components: an initial rapid temperature rise, followed by a slower and sustained heating. At the end of the initial temperature rise, a target temperature rise may have been achieved, but the cumulative nature of heat transfer means that if the process continues in time then the temperature rise may continue until the energy dissipation matches that of influx. A steady temperature increase continues until the process stops, and a sample of final temperatures can be found in Figure 5.8 which are equivalent to those process conditions found in Figure 5.7.

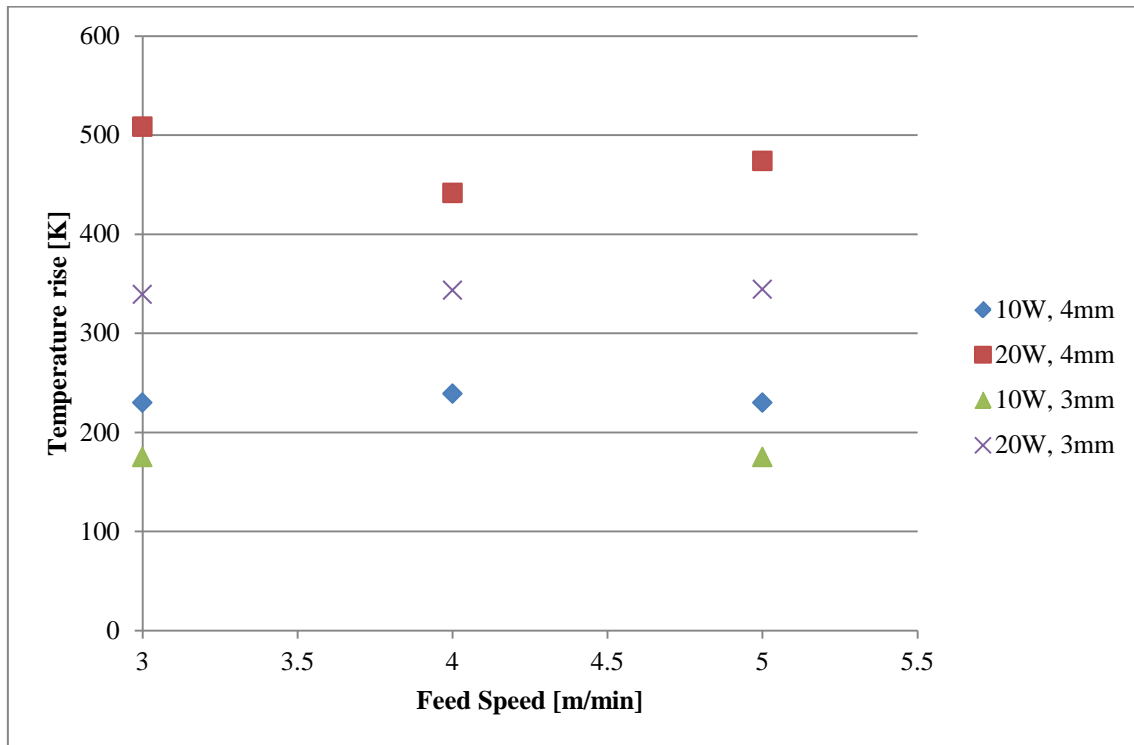


Figure 5.8: Plot of end of substrate temperature rise above room temperature induced by laser on ULE with feed speed as measured by pyrometer.

Table 5.3: Table of experimental [E] and predicted [P] temperature with variables of power and feed speed as measured by pyrometers on ULE at the initial temperature rise peak, before the gradual temperature increase component begins.

Power [W]	Feed speed [m/min]	Initial temperature peak [°C]		Max temp observed [°C]	
		Perpendicular pyrometer (10mm stand-off)		45° pyrometer at 50.4mm displacement	
		E	P	E	P
10	3	240.3	69.1	33.3	40.7
	4	252.1	62.1	33.3	35.5
	5	244.1	57.4	29.3	32.5
20	3	521.6	118.2	48.6	61.4
	4	467.7	104.2	39.2	51.0
	5	484.3	94.8	36.9	44.9

Table 5.3 contains detail of temperature measured by pyrometry and equivalent predictions.

From Table 5.3 it can be seen that the experimental and modelled results do not compare favourably for a perpendicular pyrometer at 10mm stand-off. The results are between 20% and 25% of the expected values as measured experimentally. The reason for this substantial discrepancy is uncertain; however it may be partially explained by several factors. The emissivity of the material is likely to change with temperature by an unknown quantity, which could affect measured results. The varying absorbance with temperature could also have an effect at these high temperatures.

Table 5.3 does show a more accurate model of the displaced incident angle pyrometer. As previously investigated using RTDs, the experimental values are characterised by a polynomial law. For example, the 20W dependence on feed speed is given by experimentally is given by:

$$\text{Temperature} = 3.55 * (\text{feed speed})^2 - 34.25 * (\text{feed speed}) + 119.4$$

Conversely the modelling predicts an inverse relationship for the same conditions:

$$\text{Temperature} = 174.7 / (\text{feed speed}) + 60.11$$

The true relationship between feed speed and temperature is an inverse one, as found for the theoretical results, but the experimental data does not agree. The discrepancy in the dependences is probably due to the aforementioned cooling rate issue.

### 5.3.2 SiC

The silicon carbide results, unlike those of ULE, do not take a two stage heating form. Instead, since the substrate is so reflective, the local surface quality heavily affects the substrate temperature measured by the pyrometer. To demonstrate this, Figure 5.9 contains the results for two laser powers, at 0.5m/min on a plain SiC square.

As can be seen in Figure 5.9, the temperature follows a distinct fluctuation which can only be based on the substrate surface, since all other parameters are kept constant. There is some slight desynchronisation of data due to capture time for the pyrometer being between 9-13 hundredths of a second, and not one specified time. However, it is apparent that the temperature follows the same pattern of heating with time (and therefore location on the substrate surface). The main difference in the two data series is the amplitude of the peaks, for which the higher laser power has higher temperature.

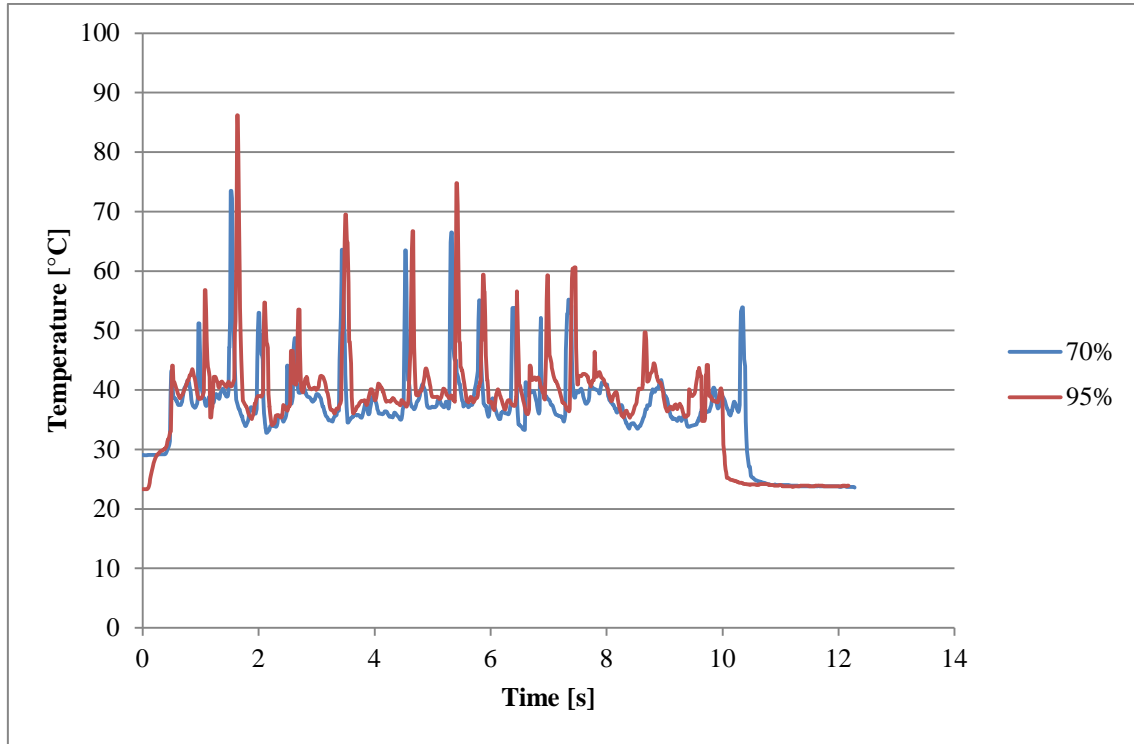


**Figure 5.9:** Plot of temperature rise induced on a SiC square by CO<sub>2</sub> laser travelling at 0.5m/min, with beam spot size of 400µm operating at different laser powers. The 70% and 95% powers correspond to 35W and 47.5W of laser power respectively. The pyrometer field of view is 6.4mmØ.

To analyse the data for the dependence of temperature on power and feed speed, a way of taking the data from the form presented in Figure 5.9 and demonstrating it more simply is required. A mean is taken of the raised temperature over time and the values of this mean are plotted in Table 5.4 for feed speeds and laser powers.

**Table 5.4: Averaged temperature rise for different feed speed/laser power configurations for a laser scan across a SiC square substrate with the same travel path (and therefore same surface quality passed over) as measured by 15mm stand-off perpendicular pyrometer.**

	0.5m/min	1.5m/min	2m/min
35W	38.09°C	36.91°C	35.86°C
47.5W	40.78°C	40.15°C	38.38°C

**Table 5.5: Table of experimental [E] and predicted [P] temperature with variables of power and feed speed as measured by pyrometers on SiC against averaged temperature rise (see Table 5.4).**

Power [W]	Feed speed [m/min]	Average temperature reached [°C]			
		Perpendicular pyrometer (10mm stand-off)		Perpendicular pyrometer (15mm stand-off)	
		E	P	E	P
35	0.5	488.6	37.3	38.1	36.5
	1.5	505.5	32.1	36.9	31.4
	2	495.5	29.9	35.9	29.3
47.5	0.5	552.1	43.4	40.8	42.4
	1.5	545.9	36.4	40.2	35.5
	2	541.5	33.5	38.4	32.7

As with ULE, the perpendicular pyrometer is not modelled to an acceptable degree of accuracy and the principle cause of this is unknown, although absorbance and emissivity varying with temperature is surely a contributor. However, these factors are highly unlikely to account for all this difference.

Again, similarly to ULE, the other pyrometer matches the model well, although in this case the pyrometer is at 15mm stand-off and perpendicular to the substrate. There is a discrepancy of no more than 6.6K with the pyrometer reading with the model. For 35W power the feed speed dependency is characterised for both data sources by a formula of the form:

$$T = m * (\text{feed speed}) + 38.9$$

The m parameter is the distinguishing factor, and is -1.44 for the experimental work, and -4.84 for the model.

### 5.3.3 Errors

The sources of error for the pyrometer work are actual equipment errors and positioning errors. The positioning errors are those introduced by the x- and y- placement of the pyrometer ( $\pm 0.50\text{mm}$ ), and the laser spot positioning ( $\pm 0.083\text{mm}$  after considering lenses). The actual errors in the equipment are the greater of  $\pm 1\text{K}$  or  $0.8\%$  inherent for the pyrometer, and power stability of the laser quoted as  $5\%$ . The three major contributors of the error are the laser spot positioning (resulting in a  $7.8\%$  temperature uncertainty), an  $8.5\%$  error induced by the pyrometer positioning and the  $5\%$  laser power (resulting in  $5\%$  uncertainty in temperature). The other factors are negligible when compared with these for their respective measurements. These combine mathematically to give a  $\pm 12.6\%$  error in pyrometer measurements.

On ULE, the pyrometry results do not fall within the experimental error, for either sampled pyrometer configuration, for previously mentioned reasons such as the cooling rate. On SiC the  $10\text{mm}$  stand-off pyrometer is a long way from the experimental error, as has previously been explained. However, for the  $15\text{mm}$  stand-off pyrometer, 4 out of the 6 sampled data above are within the experimental error, providing partial support for the modelling.

## 5.4 Thermocouples

The peak temperatures observed by thermocouples are analysed with respect to travel speed. This analysis is conducted as the nature of the heat transfer mechanism (convection and radiation combined source) of the RAP torch is different to the radiative transfer of the laser beam, meaning the two sources should have different dependences on feed speed. A plot of the relation between peak temperature as seen by the central sensor and feed speed can be seen in Figure 5.10. Similarly, a plot of the same relation for the fifth and outermost sensor for each configuration can be seen in Figure 5.11.

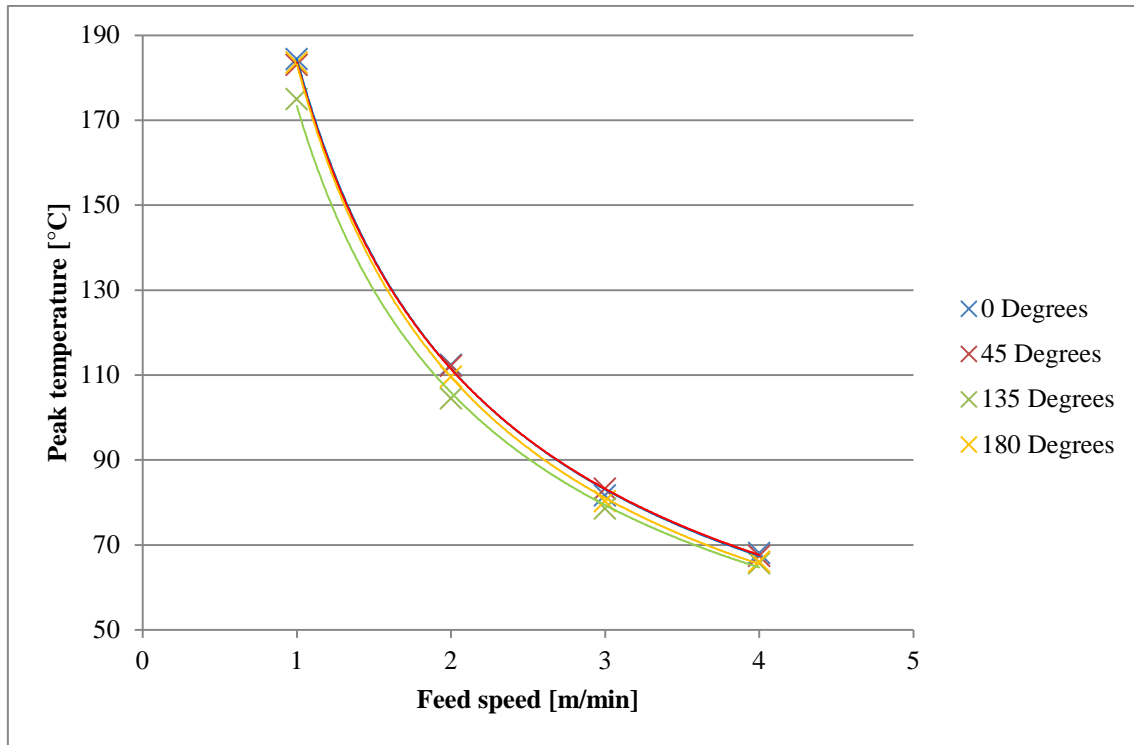


Figure 5.10: Plot of temperature with feed speed as detected by the central thermocouple during RAP processing of a Si wafer. The four separate data sets each represent different thermocouple geometry.

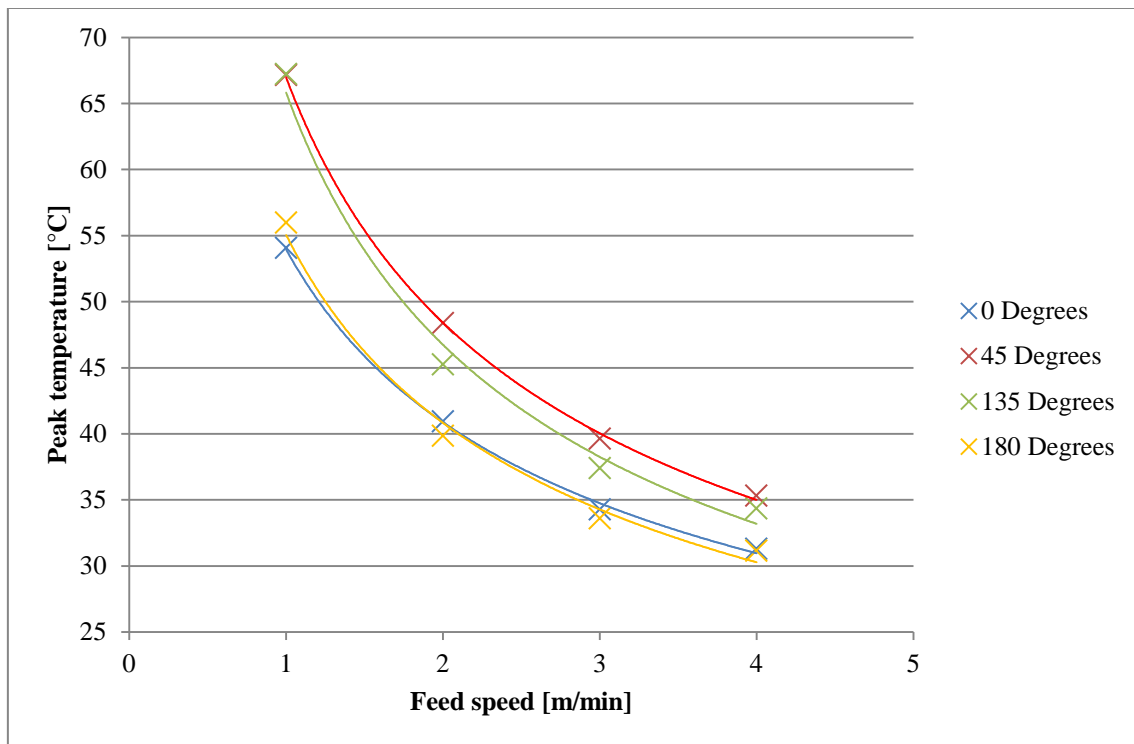


Figure 5.11: Plot of temperature with feed speed as detected by the fifth and outermost thermocouple during RAP processing of a Si wafer. The four separate data sets each represent different thermocouple geometry.

As can be seen in Figure 5.10, the feed speed of the process affects the maximum temperature achieved on the substrate by an inverse power law. The inverse power law varies with each sensor configurations but on the data points presented the power is shown to be between -0.742 and -0.711. The central sensor, for the purposes of this experiment, is treated as the pivot point for the geometric rotations, and is therefore considered to be at the same spatial coordinates for each geometry. The thermocouple may have some discrepancies induced by asymmetry of adhesive or effects of the connecting wire for different rotations – however, these factors are not known and are expected to be minimal so are treated as negligible.

When considering Figure 5.11, a similar dependence on travel speed of peak temperature observed by the furthest sensor from the torch centre path can be seen. However, the power relation between the two parameters is significantly different to that observed by the central sensor, with the power factor ranging between -0.468 and -0.401. This implies that at larger distances from the torch, the reliance of the temperature on speed is less pronounced. This is due to the summative nature of temperature – the higher surrounding temperature, coupled with the permeation of the heat through the substrate from directions other than directly perpendicular to torch travel, leads to the speed having diminished responsibility for the overall temperature at the larger distances.

Also noteworthy is the difference between two distinct geometries at the fifth sensor. This is because at the geometries known as 135° and 45° have their sensors at different distances from the torch than the other two sensors. Due to the distance between the sensors being fixed at 20mm, when angled at 45° the distances from the travel path of the torch are multiplied by  $\frac{\sqrt{2}}{2}$ , shortening their overall distance. This means they will see a slightly higher maximum temperature – the discrepancy noticeable in Figure 5.11.

The theory predicts that the temperature peak should follow the reciprocal of the feed speed, rather than following a power law as fit in this case. This kind of relationship would be based on a temperature offset and a proportionality to the reciprocal of the speed. This kind of relationship does not fit as closely to the measured data as the power law, but would explain the difference observed in the power laws between the 45°, 135° configurations and the 0°, 180° configurations. The reason a power law is a better fit in this case may be due to the scatter of the plot.

When determining the thermal map on the wafer, clearly a relationship must be ascertained of temperature with distance from the torch. In Figures 5.12 and 5.13, the highest speed is presented for the dependence of temperature on distance, namely 4m/min.

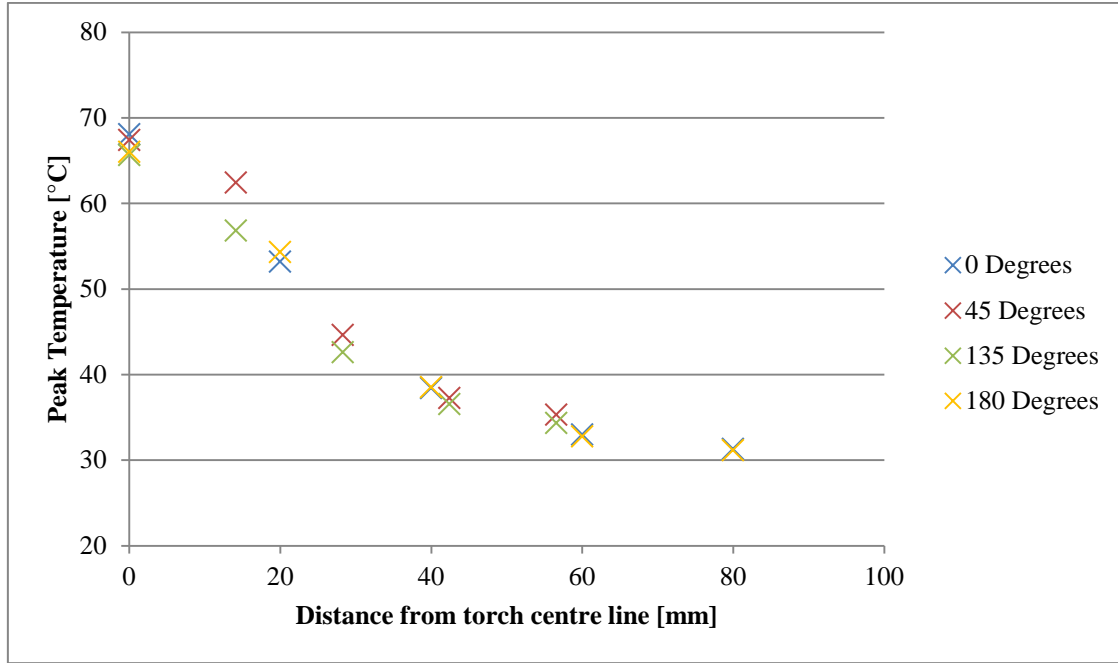


**Figure 5.12: Plot of peak temperature measured by sensors at distances from the torch centre passage using thermocouples on a SiC wafer for a RAP torch pass at 4m/min.**

Figure 5.12 presents the points themselves for each of the geometric configurations on the same axes, with colour differentiating the data sources. It is clear there is a trend defining the dependence of temperature on the distance between the torch and the sensor; however, further investigation is required to determine this relation. By assuming the distance of the sensor from the centre line as a modulus, and thus being able to also plot negative equivalents of those points, a Gaussian fit is suitable to match this data distribution: this is shown in Figure 5.13. The Gaussian fit may be suitable due to the Gaussian nature of the thermal footprint of the plasma plume. The fit is characterised by parameters below Figure 5.13.

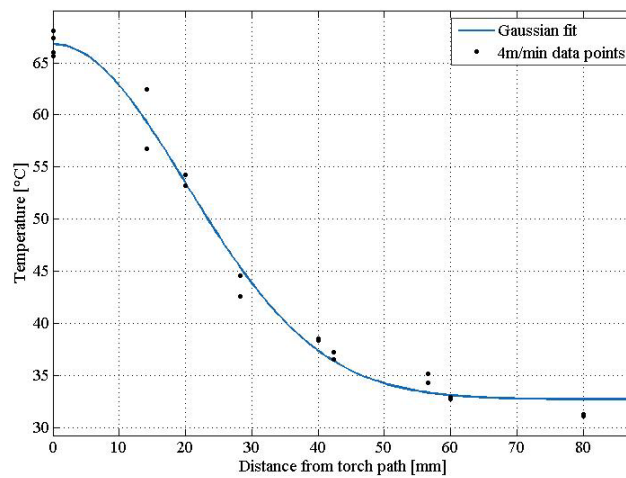


**Figure 5.13: Peak temperatures as seen in Figure 5.12 with a Gaussian curve fit to the data.**



General model:

$$f(x) = a \cdot \exp(-(x/c)^2) + d$$

Coefficients (with 95% confidence bounds):

a = 34.03 (32.8, 35.27)

c = 28.38 (26.87, 29.89)

d = 32.75 (31.83, 33.67)

Goodness of fit:

SSE: 82.04

R-square: 0.9885

Adjusted R-square: 0.9879

RMSE: 1.489

The case of the slowest investigated torch travel can be seen in Figures 5.14 and 5.15, namely 1m/min. At this speed, as expected, temperatures achieved are higher than at 4m/min at equivalent displacements. Similarly to the faster speeds, the dependence can be fitted as a Gaussian, as seen in Figure 5.15. However, the parameters characterising the dependence on distance at the slower speed is different, defined by factors below Figure 5.15.

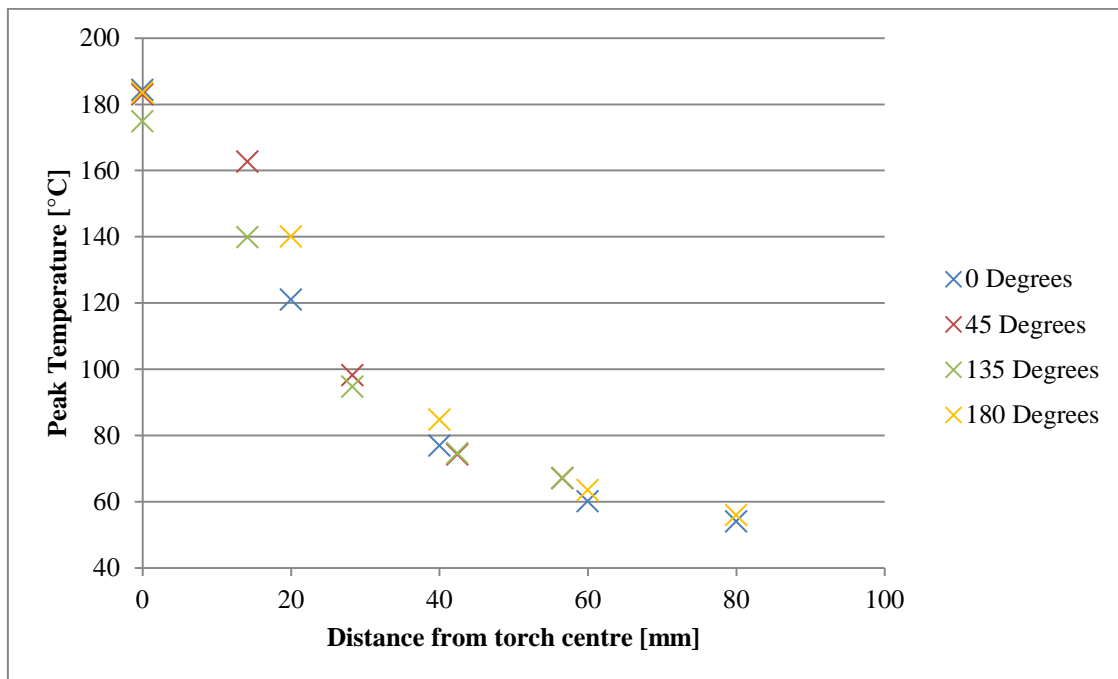
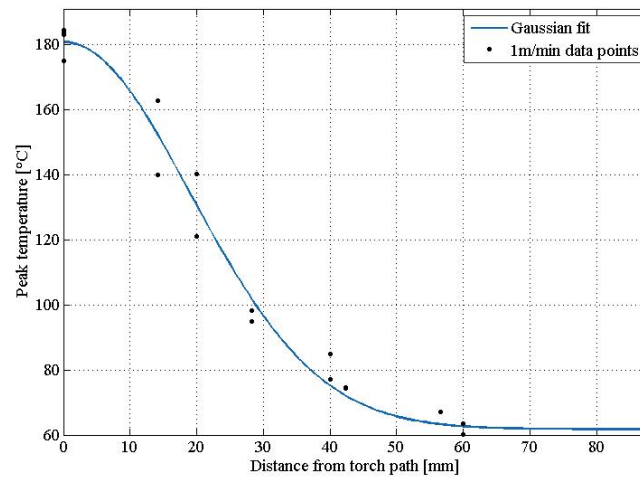


Figure 5.14: Plot of peak temperature measured by sensors at distances from the torch centre passage using thermocouples on a SiC wafer for a RAP torch pass at 1m/min.



**Figure 5.15: Peak temperatures as seen in Figure 5.14 with a Gaussian curve fit to the data.**

General model:

$$f(x) = a \cdot \exp(-((x)/c)^2) + d$$

Coefficients (with 95% confidence bounds):

$$a = 118.9 \text{ (113.5, 124.3)}$$

$$c = 27.06 \text{ (25.26, 28.86)}$$

$$d = 61.76 \text{ (57.89, 65.64)}$$

Goodness of fit:

SSE: 1604

R-square: 0.9818

Adjusted R-square: 0.9808

RMSE: 6.585

While it can be seen that there is a dependence of the peak temperature with distance, it must also be noted that due to the nature of the plasma torch and its turbulent gaseous flow, it may not be a symmetric source. To assess this, the geometries of rotational symmetry must be compared. In Tables 5.6 and 5.7, upper and lower bounds of feed speed are examined respectively. Comparison between the 0° configuration and the 180° configuration is applicable, as is a comparison between configurations at 45° and 135°.

**Table 5.6:** Table showing peak temperature values for mirrored sensor locations over the torch centre line at travel speed of 1m/min. The sensor configurations for 0 degrees and 180 degrees are symmetric about the torch pass line, as are the 45 degrees and 135 degrees lines. Sensor 1 is at the torch centre, moving out to sensor 5, which is the furthest from the substrate centre.

	Sensor	Max Temp [°C]			
		0°	180°	135°	45°
Centre	1	184.38	183.56	183.04	174.93
	2	121.05	140.09	162.69	139.92
	3	76.96	84.8	98.19	94.76
	4	60.19	63.51	74.27	74.61
Outer	5	54.07	55.97	67.14	67.21

As can be seen in Table 5.6, the central sensors have agreement to 0.82K between 0° and 180°, implying a good alignment of the substrate relative to the torch sensor. However, the second sensor sees a discrepancy of 19.04K between those sensors. This implies some inhomogeneity in the composition of the torch – it is not a perfect Gaussian. However, as the distance from the centre line of the torch increases, the asymmetry is reduced in effect, due largely to the diffusion of heat in all directions through the substrate and the heating of the surroundings leading to a more homogeneous heating of the outer regions of the substrate. Another possibility to explain the asymmetry is misalignment of the substrate. If the substrate centre was not positioned on the centre line then the sensors would have a temperature offset. Similarly, if the angle was not 45° with the centre line, the temperature would change.

The 135° and 45° thermocouple configurations follow a similar pattern, with similar peak temperatures at the centre then a significant discrepancy at the second sensor before converging in temperature terms as the outer sensor is approached. These results imply an inhomogeneity in the torch at slow speeds, with one side of the torch having a slightly different footprint than the other. However, this may not occur at faster speeds. Table 5.7 contains a similar comparison for 4m/min, the fastest speed in this case.

**Table 5.7:** Table showing peak temperature values for mirrored sensor locations over the torch centre line at travel speed of 4m/min. The sensor configurations for 0 degrees and 180 degrees are symmetric about the torch pass line, as are the 45 degrees and 135 degrees lines. Sensor 1 is at the torch centre, moving out to sensor 5, which is the furthest from the substrate centre.

	Sensor	Max Temp [°C]			
		0°	180°	135°	45°
Centre	1	68.07	66	67.41	65.66
	2	53.2	54.29	62.43	56.8
	3	38.42	38.54	44.61	42.61
	4	33	32.76	37.27	36.54
Outer	5	31.29	31.14	35.3	34.34

The results seen in Table 5.7 again follow a similar trend to the slower speeds. Conversely to the faster travel speeds however, the effects of the inhomogeneities are much less pronounced. There is a difference of no more than 5.63K (9.91% of the lower value) between symmetric pair values when at 1m/min there was up to 22.77K (16.4% of the lower value) difference for the same pair. This can be explained by the fact that there is less time for the substrate to be heated by the energy source and therefore less influence from stronger and weaker regions of the source on the footprint.

Table 5.8 shows a comparison between modelled temperatures and measured temperature values using thermocouples for a RAP torch. The thermocouple values are experimentally determined, and the modelling was performed afterwards. The reason for this is that because there is no direct analogy for ‘Power’ of the source due to the convective heat transfer, just due to the radiative component of the RAP torch as a heat source, so a power cannot be set for the model. However, by taking the measured values from the experimental work, an ‘effective power’ of the torch’s thermal footprint on the substrate can be obtained. This is an inexact science, insofar as it has no direct theoretical basis for establishing a convective power equivalency. However, it carries some meaning if it can help approximate the LAPP heat footprint using the same model.

**Table 5.8: Peak temperatures compared with their equivalent modelling results for thermocouple measurements of RAP processing of a silicon wafer for varying feed speed. The configuration modelled is the 0 degrees configuration.**

Feed speed [m/min]	Peak temperature [°C]									
	Sensor 1		Sensor 2		Sensor 3		Sensor 4		Sensor 5	
	E	P	E	P	E	P	E	P	E	P
1	184.4	186.0	121.1	124.2	77.0	90.4	60.2	67.8	54.1	52.6
2	112.4	135.3	83.4	92.2	55.5	72.8	44.4	57.9	40.9	47.7
3	81.6	114.1	62.9	80.2	43.6	65.8	36.4	53.9	34.3	45.9
4	68.1	102.1	53.2	73.7	38.4	61.9	33.0	51.7	31.3	44.9

Through trial and error, a combination of two Gaussian sources superimposed over one another was produced to tackle this problem. The two sources represent the copper nozzle of the Helios 1200 machine, a cooler and wider heat sourced, and the plasma plume itself. Taking silicon to have  $700 \text{ J.kg}^{-1}.\text{K}^{-1}$  specific heat and  $8 \times 10^{-5} \text{ m}^2.\text{s}^{-1}$  thermal diffusivity, and a ‘fully absorbed beam’ onto a  $700\mu\text{m}$  thick wafer, the model was developed. One source was modelled to have 20mm diameter and 30W equivalent power, and the other coaxial source was taken to have a 100mm diameter and 90W equivalent power. Using these conditions, the first row of results, for 1m/min feed speed, was generated.

As can be seen in Table 5.8, when the same parameters and trialled combinations were used for different feed speeds, the results became less accurate in matching the experimental results. Due to the difference in heat transfer mechanisms, the radiative aspect does not perform with the same response under changing feed speeds as a convective source, hence the discrepancy. However, it is clear that with the correct parameters for the right feed speed, a reasonable equivalency could be determined. With extensive enough investigation, a scaling factor for the feed speed could be developed and implemented to have an easily operational radiative-convective equivalency model.

#### *5.4.1 Errors*

The sources of error for the pyrometer work are actual equipment errors and positioning errors. The positioning errors are those introduced by the placement of the thermocouples relative to one another ( $\pm 0.50\text{mm}$ , resulting in a 0.8% error in temperature). The actual errors in the equipment are the greater of  $\pm 1.1\text{K}$  or 0.4% inherent for the pyrometer. The total error resulting is a  $\pm 0.9\%$  uncertainty, having taken the 0.4%, although it is more likely that the 1.1K will be used at high speeds and further distances, which with a sample low temperature could result in a percentage error of up to  $\pm 2.9\%$  on the lowest temperatures measured. However, it is clear that the uncertainty in characterising the thermal aspects of the torch is much lower than the measurements made of laser temperature. The limiting factor in the case of the torch measurements is actually the sensors themselves, as opposed to the instability of the equipment in measuring the laser.

## **6. CONCLUSIONS AND FUTURE WORK**

### **6.1 Spectrometry**

The reflectivity of a substrate has been measured for infrared wavelengths, specifically 10.6 $\mu$ m using a Fourier transform infrared spectrometer. The reflectivities of substrates were determined at 65° incidence angle, before confirmation that scattering does not adversely affect the quality of the results by measuring spherical diffuse reflection using an integrating sphere. The specific optical materials, polished Corning ULE and Trex SiC substrates, were found to have 28.5% and 93.0% reflectivity respectively at 65° incidence angle, to the nearest 0.5%.

Further work in the area of spectrometry could improve the usefulness of the reflectivity measurements for LAPP applications. The dependence of the reflectivity of the optical materials with temperature would be useful information, given that the nature of the work is to change the temperature of the substrate surface. Through appropriate modifications/accessories to the spectrometer, along with adequately sized substrate availability, the reflectivity with temperature of both materials could be determined. This information would further the understanding of the absorption properties and therefore thermal footprint of the tool on a given material.

### **6.2 Model development**

An analytical model to simulate energy beams incident on optical surfaces has been developed. The solution to the heat equations for a transient Gaussian surface source has been generated via the Green's function method. Using Matlab, codes have been written to take into account material properties, units/notation and location/shape of area being investigated. A Kirchoff transformation has been implemented so that temperature dependence of thermal conductivity can be incorporated if known. This model has been used to analyse temperatures as seen by each temperature measurement method and compared with the experimental results.

### **6.3 Laser source investigation**

The measurement of the temperature induced by a continuous wave CO<sub>2</sub> laser on the aforementioned optical materials has been performed. Two methods were selected for these measurements: resistance temperature detectors and pyrometers. Tests were devised to assess typical process parameters for laser assisted plasma processing and the resultant temperature rise for the laser energy beam component of the tool. The process

parameters treated as variables were process feed speed and laser power, because these are variable within the LAPP system.

### 6.3.1 *RTDs*

The RTD contact method was used on both SiC and ULE to identify the thermal performance of each material. The sensors were analysed at known times from the start of the laser processing, and therefore were at known distances from the spot. The data was used to develop an understanding of the equations underlying the dependences of the temperature on the process variables.

ULE was experimentally found to have a polynomial relation between temperature rise and feed speed of the process. The second order term holds a negative scalar which determines the decreasing of induced temperature with increasing speed. The constants before each term in the polynomial relation are dependent on which particular laser power is being used. Analytically modelling the same situation resulted in a predicted polynomial dependence on speed, but with a positive second order term but a negative first order term, resulting in a different predicted relationship between temperature and feed speed. It can be noted however, that these relationships are determined by fitting curves to obtained data. When examining the theory behind the process, it may be observed that the expected relationship between temperature and speed is one of inverse proportionality. This could be confirmed via fitting of different potential curves of the inverse relationship form and analysing the results as a spread from the expected form.

The measured temperature rise increased by between 25-30% with doubling of laser power, but additional analysis of this parameter is required to determine a true relationship. With analysis of all data from a certain sensor it would be possible to plot temperature against power over velocity on a single axis. This may give a closer indication of the true dependence of temperature on power when compared with the data representing the temperature variation with feed speed. The theory predicts that temperature should be directly proportional to power over feed speed, and this could be validated with the analysis suggested as part of further work.

Overall, modelling of temperature rise on ULE to match RTD sensors was successful to within 8.2K as a worst case scenario and 80% of modelled values were within 3K of their experimental counterparts.

SiC was experimentally found to have a linear relation between temperature rise and feed speed of the process. The first order term holds a negative scalar which determines the decreasing of induced temperature with increasing speed. Analytically modelling the same situation resulted in a predicted power law dependence on speed. This power law had a negative power coefficient so predicted less accurately the temperatures at low speed, by overestimating the temperature. However, these relationships were

determined using fits to the data. Theoretically, the data should fit the same dependence as specified above for ULE.

Modelling of RTD measured temperature on silicon carbide substrates was less successful than the equivalent ULE modelling. Because of the different approximation of the relation between feed speed and temperature to the experimental, it meant slow speeds (0.5m/min) overestimated temperature by 30-50%. However, at more rapid speeds (1.5 and 2m/min) the approximation using the model was much more accurate – all values fell within 3K of the experimentally measured values.

One major drawback of the results obtained using RTDs is their relatively low temperature measurements. Due to the low temperatures, the experimental error of 9.3% results in what appear to be two/three distinct values establishing part of a trend potentially being within the same error margin, casting doubt over the reliability of the measurements and the basis of the dependencies.

### 6.3.2 *Pyrometers*

The pyrometry non-contact method was used on both optical materials to determine their thermal performance. Different pyrometer configurations were used to assess the thermal footprint on the substrates of the transient laser. Of particular interest for the LAPP project as a whole was the 45° pyrometer at a 50.4mm displacement from the laser incidence zone, as this is where a pyrometer will be positioned in the LAPP machine for monitoring temperature feedback.

Using the 45° pyrometer at 50.4mm displacement, ULE was experimentally found to have a polynomial relation between temperature rise and feed speed of the process. The second order term holds a positive scalar, but the dominant term is the first order term which has a negative scalar, determining the decreasing of temperature with increasing feed speed. The constants before each term in the polynomial relation are dependent on which particular laser power is being used. Analytically modelling the same situation resulted in a predicted inverse relationship between speed and temperature. The discrepancies between modelled and experimental values is most likely due to the cooling rate of the substrate by the surroundings from the top surface, a factor not accounted for in the model. With regards to the power dependence of temperature, the model has a stronger dependency on power than the experimental results. The model predicts a linear relation of power and temperature, with temperature rise from room temperature doubling with doubling power. Experimentally, there is no clear trend in the dependence found, ranging between 40% and 115% increase from room temperature found. It is clear that to determine the relation fully, further experimentation needs to be conducted.



Overall the results for the 45°, 50.4mm displacement pyrometer between model and experimental match to within 12.8K. However, at a power of 10W the temperature difference is at worst 7.4K. The match between the prediction and measured data is improved at higher speeds as well, with 5m/min achieving 3.2K difference. The cooling rate factor previously mentioned may rectify the differences between modelling and experimental to a level accurate enough to reliably utilise this model to predict temperatures for this pyrometer, to  $\pm 2^\circ\text{C}$  sufficing.

The experimental results for the perpendicular pyrometer are much higher than the modelled results, with the modelled results consistently predicting between 20-25% of the maximum temperature measured. The principle cause for this discrepancy is unknown, but may be partially attributed to variation of material emissivity and absorption with temperature, as well as variation of other material properties with temperature such as thermal conductivity.

Silicon carbide's temperature rise was found, using a pyrometer to be reliant on local surface quality. The induced temperature was found to follow a specific pattern with time as the spot traversed the substrate surface, implying a specific relation of absorption with surface location. Even on a high quality substrate such as the Trex SiC square used which had sub-nanometre surface figure error from the flat, the variation in reflectivity with distance can mean a temperature variation of over 50K across the surface. This means that an assumption must be made that the average temperature matches the reflectivity measured previously using spectrometry for the purposes of modelling.

Using a pyrometer at 15mm stand-off, a dependency of temperature on feed speed has been determined to be linear on SiC, with temperature decreasing with increasing feed speed. The model predicts a linear relationship as well, but has a different scaling factor in front of the first order term, resulting in a more rapid decrease of temperature with speed. These results are matched by less than 6.6K difference between modelling and prediction consistently over the range of feed speeds selected.

The 10mm stand-off perpendicular pyrometer, in a similar manner to the ULE measurements, was found to give very high temperature readings compared with the model. The modelled results are <10% of the temperature of the measured data. This is clearly not an accurate model, and the main explanation for the discrepancy is not known. The reasons suggested for this discrepancy are the same as previously suggested for ULE.

## 6.4 RAP source investigation

A silicon wafer was used to assess the thermal profile of a RAP torch, specifically that in the Helios 1200 machine. Thermocouple contact sensors were adhered to the substrate rear to measure temperature without damage or interference from the plasma. Several geometries were used to ascertain different aspects of the torch.

A symmetry assessment of the RAP torch was conducted by using symmetric geometries of sensors. Temperature measured by sensors at the outer regions of the substrate had good agreement with one another, to within 3K for the last two sensors. This implies homogeneity is not an issue at increased distance from the torch. However, at closer distances (20mm and 40mm) there were inhomogeneities of up to 16% (or 22K). Further work into this kind of investigation would be to utilise a thermal camera to image the thermal footprint on the back of the substrate whilst maintaining a safe distance away from the plasma and observe any inhomogeneities and how these may behave with feed speed variation.

The dependence of the temperature measured by thermocouples on the feed speed of the process was found experimentally to be an inverse power law. This fitted power law is really a discrepancy from what should be an inverse relation between feed speed and temperature. The scaling of the power term and the power to which the relation is raised varies with the distance of the sensor from the centre line. The dependence of temperature on feed speed is less pronounced at greater distances from the centre line, and this is believed to be due to the summative nature of temperature. The higher surroundings temperature and permeation of heat through the substrate will reduce the overall dependence on the feed speed.

With the temperature measured depending on distance from the centre line, obviously a key factor in determining the size of the etch profile of the RAP process from the thermal aspects of the process, this variation was examined. Different feed speeds were examined, but for each feed speed the dependence of the temperature on displacement from torch centre was found to best fit a Gaussian shaped temperature distribution over the set of speeds measured. The Gaussian was offset by a base temperature level for each speed.

When attempting to model the temperature induced on the Si wafer with the analytical model, a Gaussian heat source did not adequately match the temperature profile on the substrate. However, it was found that by a superposition of two modelled Gaussian sources, the temperature distribution with distance could be matched for a specific speed. This is thought to be because of the additional heat component arising from the copper nozzle of the torch. Due to the nature of the heating mechanism of the RAP torch being different to the radiative source of the model, there must be a scaling factor applied to each different feed speed modelled to match the experimental values, as can be observed from the increasingly inaccurate modelling with varying feed speed

increase. However, at a specified feed speed (1m/min), the model was found to match to within 1.6, 3.1, 13.4, 7.6, and 1.5K for sensors 1-5 respectively. The discrepancy was larger for the middle sensors because this is where the dominance of the Gaussian sources in the model reverses, but with some adjustment of the parameters this could be improved. Thus far the investigation into this phenomenon is rudimentary, but with further work on investigating parameters the model could become a rather elegant approximation of a combined convective and radiative heat source.

### **6.5 Additional further work**

The key improvement that could be made to the modelling efficiency in predicting temperature is an accounting for the cooling rate of substrates. Due to convection, conduction and radiation of heat from the surface of the substrate, the temperatures predicted are not as accurate as they could be, in particular for high temperatures, and also for the dependences on feed speed. The model currently only accounts for conduction of the heat through the substrate itself, which is not the case. With further research into this topic, the equations and code could be improved to increase accuracy.

Additionally, to better understand the localised distribution of temperature on the substrate surface, more non-contact methods could be implemented. Specifically, a thermal imaging camera could be used to observe the profile at known times and the model could be compared with these images to try to match distributions of temperature to the results. This information would help to improve the modelling on a point by point basis, improving the x-y accuracy of the temperature and thus the thermal footprint.

To further investigate the effects of the RAP torch using thermocouples, an interesting set of tests would involve the optical materials in substrate dimensions similar to the Si wafers. The thermocouples could be attached to the rear surfaces of the optical substrates and a similar set of tests to those already could be conducted to observe the thermal profile distribution due to a RAP torch on more applicable substrates.

Perhaps the most important set of tests would be devised to be used in the LAPP machine. With the wafer-like substrates mentioned in the previous paragraph, along with the thermocouples on the rear, LAPP of the substrates could be measured for their thermal properties. With the pyrometer placed at 50.4mm and 45° within the machine with its protective shielding, and the thermocouples on the substrate rear, as much thermal information about the process as possible could be determined experimentally. This could then be utilised by combining the model variations used for the RAP torch and the laser source, and refining the predicted temperatures. Since these optical substrates would have been LAPP etched, the substrates could then be analysed for their

etched surface profiles, and the thermal data used alongside the material removal data to explain etch rates with temperature of the new LAPP system. This could then be used to more accurately predict how surfaces would respond to LAPP, and save time and money in characterising the system for different materials.

## 7. REFERENCES

- [1] Lawrence Livermore National Laboratory, *Building NIF: An Engineering Marvel*, available at: [https://lasers.llnl.gov/about/nif/building\\_nif/engineering\\_marvel.php](https://lasers.llnl.gov/about/nif/building_nif/engineering_marvel.php) (accessed 26/06/2012).
- [2] Liske, J. (15/6/2012), *Brief summary of the E-ELT project*, available at: [http://www.eso.org/sci/facilities/eelt/docs/E-ELT\\_2012-06-15.pdf](http://www.eso.org/sci/facilities/eelt/docs/E-ELT_2012-06-15.pdf) (accessed 20/06/2012).
- [3] Fanara, C., Shore, P., Nicholls, J. R., Lydford, N., Sommer, P. and Fiske, P. (2006), "A new Reactive Atom Plasma Technology (RAPT) for precision machining: The etching of ULE® optical surfaces", *Advanced Engineering Materials*, vol. 8, no. 10, pp. 933.
- [4] Gurnett, D. A. and Bhattacharjee, A. (2005), *Introduction to plasma physics: with space and laboratory applications*, Illustrated, reprint ed, Cambridge University Press, Cambridge, UK.
- [5] Boyd, T. J. M. and Sanderson, J. J. (2003), *The Physics of Plasma*, illustrates ed, Cambridge University Press, Cambridge, UK.
- [6] Boulos, M. I. (1985), "INDUCTIVELY COUPLED R. F. (RADIO FREQUENCY) PLASMA.", *Pure and Applied Chemistry*, vol. 57, no. 9, pp. 1321-1352.
- [7] O'Brien, W. J. (2011), *Characterisation and Material Removal Properties of the RAP<sup>TM</sup> Process* (unpublished Ph.D. thesis), Cranfield University, Cranfield University.
- [8] Boumans, P. W. J. M. (1979), "Inductively coupled plasma-atomic emission spectroscopy: Its present and future position in analytical chemistry", *Fresenius' Zeitschrift für Analytische Chemie*, vol. 299, no. 5, pp. 337-361.
- [9] Arnold, T., Böhm, G., Eichentopf, I. -, Janietz, M., Meister, J. and Schindler, A. (2010), "Plasma Jet Machining", *Vakuum in Forschung und Praxis*, vol. 22, no. 4, pp. 10.
- [10] Jourdain, R., Marson, S., Shore, P., Sparkes, M. and O'Neill, W. (2011 Unpublished), *Laser Assisted Plasma Process, WP1: Process Technical Review*, WP1, -, -.
- [11] Barnett, F. R. and Norr, M. K. (1973), "Carbon fiber etching in an oxygen plasma", *Carbon*, vol. 11, no. 4, pp. 281-284, IN1-IN8, 285-288.

- [12] Castelli, M., Jourdain, R., Morantz, P. and Shore, P., ( 2012), *Reactive Atom Plasma for rapid figure correction of optical surfaces*, Liverpool, Merseyside ed.
- [13] Rossnagel, S. M., Cuomo, J. J. and Westwood, W. D. (1990), ***Handbook of plasma processing technology : fundamentals, etching, deposition, and surface interactions***, illustrated, reprint ed, William Andrew.
- [14] Winters, H. F. and Coburn, J. W. (1992), "Surface science aspects of etching reactions", *Surface Science Reports*, vol. 14, no. 4-6, pp. 161-269.
- [15] Takino, H., Shibata, N., Itoh, H., Kobayashi, T., Tanaka, H., Ebi, M., Yamamura, K., Sano, Y. and Mori, Y. (1998), "Plasma chemical vaporization machining (CVM) for fabrication of optics", *Japanese Journal of Applied Physics, Part 2: Letters*, vol. 37, no. 7 SUPPL. B, pp. L894-L896.
- [16] Eichentopf, I. -, Böhm, G., Meister, J. and Arnold, T. (2009), "Reactive plasma jet high-rate etching of SiC", *Plasma Processes and Polymers*, vol. 6, no. SUPPL. 1, pp. S204.
- [17] Yao, Y. X., Wang, B., Wang, J. H., Jin, H. L., Zhang, Y. F. and Dong, S. (2010), "Chemical machining of Zerodur material with atmospheric pressure plasma jet", *CIRP Annals - Manufacturing Technology*, vol. 59, no. 1, pp. 337-340.
- [18] Eichentopf, I. -, Böhm, G. and Arnold, T. (2011), "Etching mechanisms during plasma jet machining of silicon carbide", *Surface and Coatings Technology*, vol. 205, no. SUPPL. 2, pp. S430.
- [19] Mori, Y., Yamauchi, K., Yamamura, K. and Sano, Y. (2000), "Development of plasma chemical vaporization machining", *Review of Scientific Instruments*, vol. 71, no. 12, pp. 4627-4632.
- [20] Yamamura, K., Morikawa, T., Ueda, M., Nagano, M., Zettsu, N. and Shibahara, M. (2009), "Highly efficient damage-free correction of thickness distribution of quartz crystal wafers by atmospheric pressure plasma etching", *IEEE transactions on ultrasonics, ferroelectrics, and frequency control*, vol. 56, no. 6, pp. 1128-1130.
- [21] Li, N., Wang, B. and Jin, H. L. (2012), "Study on atmospheric pressure plasma processing in contactmode", in Shore, P., Spaan, H. and Burke, T. (eds.), *Proceedings of the 12th international conference of the european society for precision engineering and nanotechnology*, Vol. 2, 4th-7th June 2012, Stockholm, euspen, pp. 493.
- [22] Golini, D., Kordonski, W. I., Dumas, P. and Hogan, S. (1999), "Magnetorheological finishing (MRF) in commercial precision optics manufacturing", *Proceedings of the 1999 'Optical Manufacturing and Testing III'*, Vol. 3782, 20 July 1999 through 23 July 1999, Denver, CO, USA, Society of Photo-Optical Instrumentation Engineers, Bellingham, WA, United States, pp. 80.

- [23] DeGroote, J. E., Marino, A. E., Wilson, J. P., Bishop, A. L., Lambropoulos, J. C. and Jacobs, S. D. (2007), "Removal rate model for magnetorheological finishing of glass", *Applied Optics*, vol. 46, no. 32, pp. 7927-7941.
- [24] Jacobs, S. D., Yang, F., Fess, E. M., Feingold, J. B., Gillman, B. E., Kordonski, W. I., Edwards, H. and Golini, D. (1997), "Magnetorheological finishing of IR materials", *Optical Manufacturing and Testing II*, Vol. 3134, 27 July 1997 through 27 July 1997, San Diego, CA, pp. 258.
- [25] Demmler, M., Zeuner, M., Allenstein, F., Dunger, T., Nestler, M. and Kiontke, S. (2010), "Ion Beam Figuring (IBF) for high precision optics", *Advanced Fabrication Technologies for Micro/Nano Optics and Photonics III*, Vol. 7591, 25 January 2010 through 27 January 2010, San Francisco, CA, .
- [26] Shanbhag, P. M., Feinberg, M. R., Sandri, G., Horenstein, M. N. and Bifano, T. G. (2000), "Ion-beam machining of millimeter scale optics", *Applied Optics*, vol. 39, no. 4, pp. 599-611.
- [27] Steen, W. M. (2003), "Laser material processing - An overview", *Journal of Optics A: Pure and Applied Optics*, vol. 5, no. 4, pp. S3-S7.
- [28] Williams, C. (1997), "CO2 laser processing - an overview", *Aircraft Engineering and Aerospace Technology*, vol. 69, no. 1, pp. 43-52.
- [29] Schaaf, P. (2010), *Laser Processing of Materials: Fundamentals, Applications and Developments*, Springer.
- [30] Siegman, A. E. (1986), "Wave Optics and Gaussian Beams", in *Lasers*, Illustrated, reprint ed, University Science Books, , pp. 626.
- [31] , *Super-sharp lasers to boost disc capacity tenfold*(2006), available at: <http://pinktentacle.com/2006/06/super-sharp-lasers-to-boost-disc-capacity-tenfold/> (accessed 12/03/12).
- [32] Hoffman, J., Mościcki, T. and Szymański, Z. (2003), "Laser beam-plasma plume interaction during laser welding", in Wolinski W.L., Jankiewicz Z. and Romaniuk R. (eds.), *Laser Technology VII: Applications of Lasers*, Vol. 5229, 23 September 2002 through 27 September 2002, Szczecin-Swinoujscie, pp. 228.
- [33] Acheson, D. J. (1990), *Elementary Fluid Dynamics*, illustrated, reprint ed, Oxford University Press, Oxford.
- [34] Weiner, J. and Ho, P. -. (2008), *Light-Matter Interaction, Fundamentals and Applications*, John Wiley & Sons.
- [35] Lax, M. (1977), "Temperature rise induced by a laser beam", *Journal of Applied Physics*, vol. 48, no. 9, pp. 3919.

- [36] Lax, M. (1978), "Temperature rise induced by a laser beam II. the nonlinear case", *Applied Physics Letters*, vol. 33, no. 8, pp. 786.
- [37] Cline, H. E. and Anthony, T. R. (1977), "Heat treating and melting material with a scanning laser or electron beam", *Journal of Applied Physics*, vol. 48, no. 9, pp. 3895.
- [38] Nissim, Y. I., Lietoila, A., Gold, R. B. and Gibbons, J. F. (1980), "Temperature distributions produced in semiconductors by a scanning elliptical or circular cw laser beam", *Journal of Applied Physics*, vol. 51, no. 1, pp. 274.
- [39] Manca, O., Minea, A. A., Nardini, S. and Tamburrino, S. (2010), "Transient heat conduction in solids irradiated by a moving heat source with combined donut and gaussian distributions", *International Review of Mechanical Engineering*, vol. 4, no. 2, pp. 123-127.
- [40] Manca, O., Nardini, S., Ricci, D. and Tamburrino, S., ( 2011), *Numerical simulation of transient temperature fields in solids irradiated by moving gaussian and donut sources*, Paris ed.
- [41] Loza, P., Kouznetsov, D. and Ortega, R. (1994), "Temperature distribution in a uniform medium heated by linear absorption of a Gaussian light beam", *Applied Optics*, vol. 33, no. 18, pp. 3831-3836.
- [42] Loze, M. K. and Wright, C. D. (1997), "Temperature distributions in semi-infinite and finite-thickness media as a result of absorption of laser light", *Applied Optics*, vol. 36, no. 2, pp. 494-507.
- [43] Lu, Y. - and Aoyagi, Y. (1995), "Temperature rise and heat flux induced by laser beam with double-Gaussian intensity distribution", *Japanese Journal of Applied Physics, Part 1: Regular Papers & Short Notes & Review Papers*, vol. 34, no. 7A, pp. 3759.
- [44] Lu, Y. F., Loh, T. E., Soh, H. G. and Low, T. S. (1995), "Laser-induced temperature rise in Gaussian-shaped holes", *Applied Surface Science*, vol. 90, no. 2, pp. 217.
- [45] Omega Engineering Inc. , *OMEGAFILM Platinum RTD sensors*, available at: [http://www.omega.com/Temperature/pdf/F1500\\_F2000\\_F4000.pdf](http://www.omega.com/Temperature/pdf/F1500_F2000_F4000.pdf) (accessed 02/02/2012).
- [46] Pico Technology , *Thermocouple application note*, available at: <http://www.picotech.com/applications/thermocouple.html> (accessed 10/12/2011).
- [47] LumaSense Technologies , *IMPAC Infrared Thermometers*, available at: <http://www.contika.dk/Download/brochurer/impac/in510.pdf> (accessed 20/9/2011).



- [48] FLIR Systems , *FLIR A615*, available at:  
[http://www.flir.com/uploadedFiles/Thermography\\_APAC/Products/Product\\_Literature/100930%20A615%20datasheet\\_en.pdf](http://www.flir.com/uploadedFiles/Thermography_APAC/Products/Product_Literature/100930%20A615%20datasheet_en.pdf) (accessed 15/02/2012).